

$$AFORD = TD = 76 = \overline{1568}$$

10

## AFOSR Interim Scientific Report

AFOSR-TR-76-

12

## Experiments and Analysis Related to External Burning for Propulsion

Prepared for

Air Force Office of Scientific Research  
Aerospace Sciences Directorate  
Bolling Air Force Base, D. C.

by

James E. Hubbartt  
Warren C. Strahle  
Douglas H. Neale  
Walter W. Wilson

School of Aerospace Engineering  
Georgia Institute of Technology  
Atlanta, Georgia 30332

Approved for public release; distribution unlimited  
Grant No. AFOSR 75-2794 March 1976

Conditions of Reproduction  
Reproduction, translation, publication, use and  
disposal in whole or in part by or for the United  
States Government is permitted.

AFOSR Interim Scientific Report

AFOSR-TR-76-

Experiments and Analysis Related  
to External Burning for Propulsion

Prepared for

Air Force Office of Scientific Research  
Aerospace Sciences Directorate  
Bolling Air Force Base, D. C.

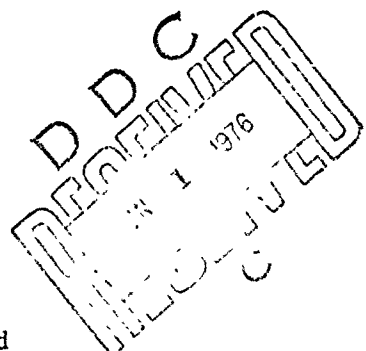
by

James E. Hubbard  
Warren C. Strahle  
Douglas H. Neale  
Walter W. Wilson

School of Aerospace Engineering  
Georgia Institute of Technology  
Atlanta, Georgia 30332

Approved for public release; distribution unlimited  
Grant No. AFOSR 75-2794

March 1976



Conditions of Reproduction

Reproduction, translation, publication, use and  
disposal in whole or in part by or for the United  
States Government is permitted.

### Abstract

The results of first year's efforts on an experimental base flow program are reported. The design and checkout for a Mach 3.0 axisymmetric wind tunnel with a model base diameter of 2.25 inches is described, as well as the automated data acquisition system. Experiments are reported on detailed static pressures for the diffuser wall, model wall and base and near wake. Temperature measurements are presented to establish a near adiabatic wall condition. The relationship between the experimental program and propulsive external burning is discussed.

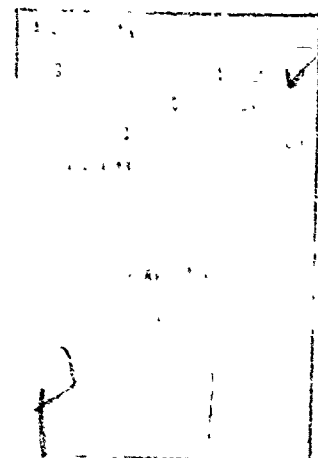


TABLE OF CONTENTS

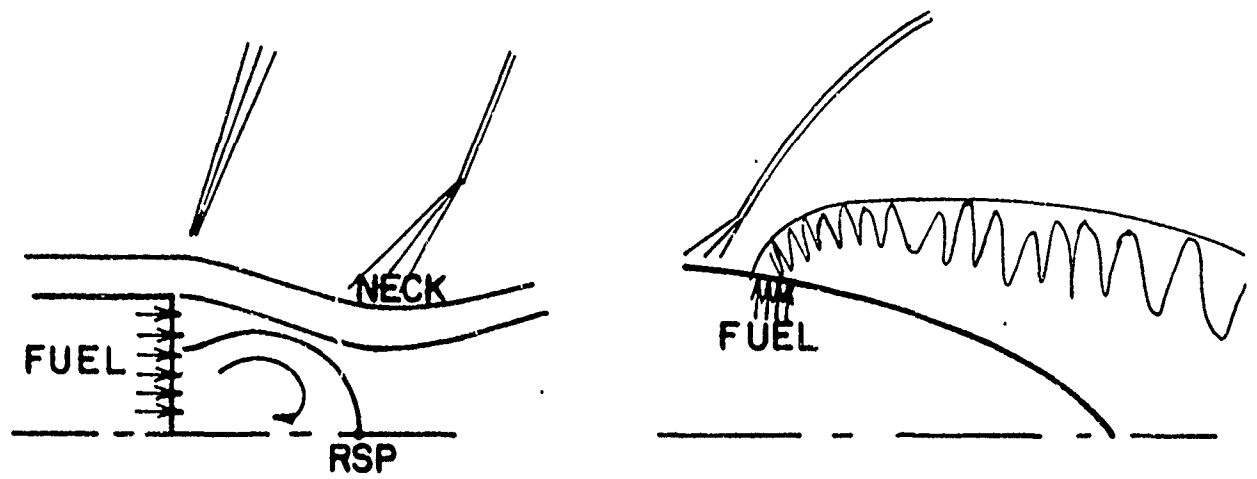
	Page
Abstract	i
Table of Contents	ii
Chapters	
I. Introduction	1
II. Test Facility	10
III. Results of Flow and Data Evaluation Tests	34
IV. Base Flow Results	48
References	56

## CHAPTER I

### INTRODUCTION

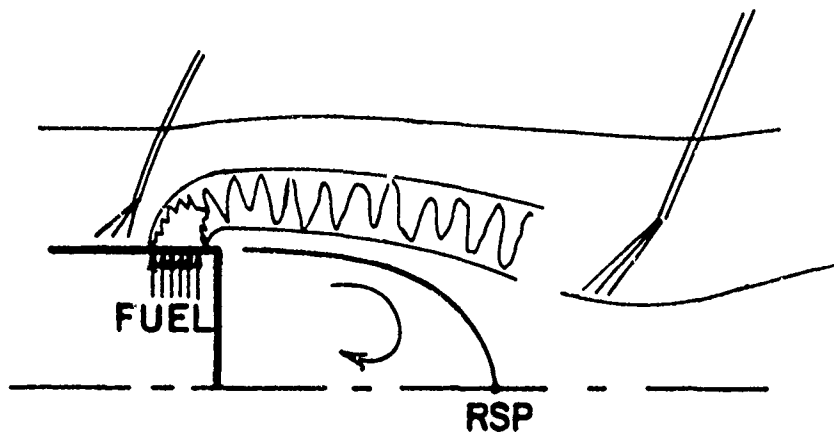
There are a great number of potential air-to-air, air-to-ground, and ground-to-air weaponry missions that require either a sustain or mild acceleration phase of the missile trajectory or which could benefit from a substantial drag reduction during a portion of the trajectory. Furthermore, many of these missions require operation sufficiently low in the atmosphere that airbreathing propulsion, if it is competitive with the rocket, is attractive. Recent concepts of external burning for propulsion appear attractive for these missions because it is possible to make these systems extremely simple, essentially eliminating the requirement for an inlet, combustion chamber and nozzle, at an acceptable sacrifice of  $I_{sp}$  compared with usual airbreathing systems. At the present time, there is experimental proof that the concept will work, but the ability to scale and predict is not available with any precision. The experimental facility described herein is designed to provide experimental proof that an analytical model currently under development will actually predict the effects on base pressure of many processes which take place during external burning.

Historically, the concept of external burning for propulsion appears to have evolved through three phases, all subsequent to a firm understanding of supersonic flight, with the last phase dependent upon preliminary understanding of base flows. The three phases are tied to the three concepts shown in Figure 1. The initial attempts at the manipulation of the base flow operated upon base-bleed combustion, shown in Figure 1a. Combustion, confined to the



a. BASE BLEED COMBUSTION

b. COMBUSTION ADJACENT TO  
AN AFTERBODY



c. COMBUSTION ADJACENT TO THE NEAR WAKE

FIGURE I. CONCEPTS OF EXTERNAL COMBUSTION FOR  
PROPELLSION.

recirculating flow field or in the shear layer between the inviscid flow-field and the recirculating flow, has its main action upon the total pressure of the flow in the shear layer. In all cases base pressure is determined by the downstream condition that the flow must pass into a far wake condition. Consequently, the flow in the shear layer above the stagnating stream must have sufficient momentum to negotiate the compression turn near the axis. Base-bleed combustion operates by increasing the static and total temperatures of the flow in the shear layer. Increasing the temperature increases the speed of sound. Since the velocity field is fairly well fixed by the exterior inviscid flow and the low velocity recirculating flow, the effect of combustion is to reduce the average Mach number in the shear layer. Since the static pressure is bounded by the free stream static pressure, the net effect of combustion is to decrease the total pressure of the shear layer and its ability to undergo a reattachment pressure rise. Consequently, the base pressure, which is the initial condition for the wake flow, cannot be small; it must rise toward the free stream static pressure as combustion raises the temperature.

This effect was indeed found in References (1) and (2). In the work of Baker et. al.<sup>(1)</sup> injection and spark ignition of  $H_2$  in the base flow region was carried out at a free stream Mach number of 1.9 on a projectile with a 2.25 inch base diameter. The free stream static pressure was atmospheric, and, when burning occurred, the base pressure rise maximized around 6 psi, or to a level about 2 psi below atmospheric. Defining the specific impulse as the change in base-force level divided by the hydrogen mass-flow rate, the  $I_{sp}$  peaked at about 1000 sec. The thrust produced by the hydrogen jets themselves exhausting through ports in the base, was negligible compared to the thrust increase due to base burning.

In the work of Scanland and Hebrank,<sup>(2)</sup> 40-mm rounds were loaded with a pyrotechnic that exhausted through the base. Effects on drag were measured by observing the flight of a fired round. At  $M_\infty = 1.65$ , it was concluded that 65% of the base drag was eliminated by a flow rate of roughly 0.027 lb/sec, or an  $I_{sp}$  of roughly 180 sec was attained.

Work on this concept was renewed in the late 1960's, as given in References (3) and (4). Townsend and Reid<sup>(3)</sup> bled  $H_2$  gas around the entire periphery, normal to the free stream, near the base of a 1.0-inch diameter projectile. The test conditions were  $M_\infty = 2.16$  and  $P_\infty = 3$  psi. Spark ignition was used and the maximum  $I_{sp}$  was approximately 3600 sec, but again, the base pressure rise was limited. It was found that the base pressure could only be raised slightly higher than the body static pressure forward of the injection ring. Experiments were run with and without a conical afterbody, but no essential difference in results was found, since the base flow was separated regardless of the afterbody presence. The theoretical work of Davis<sup>(4)</sup> showed clearly that the above-mentioned mechanism is responsible for the base pressure rise and theoretically explained the order of magnitude of the  $I_{sp}$  attainable with  $H_2$ . While the  $I_{sp}$  levels are attractive with base-bleed combustion, it is quite clear that these magnitudes can only be attained at low base pressure rises. Base injection may be thought of as a mass addition and heat generation in the near wake, and it is now quite clear what the gross effects should be.<sup>(5-7)</sup> These manipulations do not change the condition that the flow must ultimately reattach to a stream characterized by  $P_\infty$ . They only change the ability to withstand a reattachment pressure rise within the constraint imposed by  $P_\infty$ . The limitation on base pressure clearly becomes the free stream static pressure.

The second phase, augmented by the theoretical work of References (8-10), was initiated during the middle 1950's and is summarized in the unclassified literature in Reference (11). The concept of external burning adjacent to boattail afterbodies is shown in Figure 1b. Except for a combustion strength sufficient to cause massive separation, no limitation appears on the base pressure rise attainable with this method, presuming also that the flowfield does not become subsonic through the action of heat addition. A maximum thrust  $I_{sp}$  of 818 sec has been obtained on a 20° half-angle wedge using triethylaluminum (TEA) as a fuel at Mach 5.0. The majority of results were far lower than this value, however, due to combustion difficulties in the wind tunnel facilities available at the time. In any event, a primary drawback to the method, for many missions, is the requirement of an afterbody. Furthermore, extensive separation may be induced at large pressure rises, and this may be objectionable from a controls standpoint.

Concept b) of Figure 1 operates on the known principle of heat addition to a supersonic flow that streamlines diverge under the heating action. This in turn causes a pressure increase in supersonic flow. Not surprisingly, this method produces an  $I_{sp}$  of roughly  $\frac{1}{2}$  that of a SCRAMJET at the same combustor conditions, because  $\frac{1}{2}$  of the thrust surface is thrown away; that is, there is no outer wall containing the combustion. It is only through manipulation of the inviscid flowfield that large pressure rises may occur. Usually, mission requirements are such that only partial drag relief does not justify the incorporation of a propulsion system; consequently, large pressure rises are required by an external burning system.

It was Strahle<sup>(12)</sup> who first introduced the concept shown in Figure 1c,

which led into the third phase of investigation of external burning for propulsion. Strahle was the first to systematically explore the possibility of raising the base pressure behind bluff-base bodies by combustion in the exterior inviscid flow. An indication that this method is feasible was given by Serafini et. al.<sup>(13)</sup> Aluminum borohydride was injected at discrete points perpendicular to the flow at a station 10.5 inches from the nose of revolution 21 inches long. The Mach number was 2.47 at a pressure altitude of 55,000 feet. A net thrust condition was observed and the base specific impulse was roughly 200 sec. This result is open to question because of possible tunnel interference, but the nature of this interference was never explicitly shown.

The primary idea in this concept is that there is a base flow mechanism for transmission of high downstream pressures upstream to the base, because of the subsonic recirculation zone. Consequently, an afterbody is not required, and for many vehicles it is not desired anyway. Although it is an oversimplification, one way of viewing this concept is an entrapment of the subsonic region in a zone of high pressure caused by combustion. The actual mechanism is intimately involved with the reattachment process, however.

Several classified programs have followed the work of Reference (12) in an attempt to provide an experimental basis for the concept. While the results cannot be discussed in detail because of classification difficulties, it may be stated that it is not proved that the base pressure may be raised above the free stream static pressure and the  $I_{sp}$  values are substantially in excess of rocket engine values. A major improvement on the concept was added by the Atlantic Research Corporation. In Reference (12) it was tacitly

assumed that the fuel would be a pyrophoric liquid. Practically, this leads to difficulties at small size scales in obtaining an axisymmetric ring of fuel with large air capture. ARC introduced the concept of using a solid propellant gas generator as the fuel generator. Since the mass flow per unit area of a gas is lower than that of a liquid, larger injection ports may be used and the fuel better distributed about the body periphery. Furthermore, the usual advantages of solids over liquids are apparent.

The theory of Reference (12) was based upon a highly simplified picture of the process, using the two dimensional Crocco-Lees<sup>(12)</sup> theory of base flows and confining combustion to the inviscid flow. In practice, combustibles will become entrained in the shear layer and the concept will operate as a mixture of concepts a) and c) in Figure 1. No analysis exists capable of treating these phenomena. Given impetus by the field of wake observables, much has been done in recent years concerning analysis of near wakes.<sup>(6,15)</sup> Nevertheless, no analysis yet exists, except for a reasonably inaccurate older theory,<sup>(16)</sup> of the axisymmetric, turbulent base flow with a non-adiabatic condition on the shear layer.

For adiabatic shear layers with external combustion, recent theory and experiment have become available from the U.S. Naval Postgraduate School.<sup>(17-19)</sup> Experiments at Mach 2 have been carried out simulating external burning by compression waves generated by the nozzle wall contour. Base pressure was the single parameter measured and the theoretical treatment of the Crocco-Lees theory,<sup>(14)</sup> modified for axial symmetry, and using the method of characteristics in the inviscid stream. Cold gas injection through the base was investigated in conjunction with externally generated pressure waves. In this program it was found that a) net thrust could be expected to be produced by external burning, b) it was advantageous to locate the heat release

region so that compression waves impinged slightly forward of the base, c) the shorter the length of the effective heat release zone for a fixed heat release, the better and d) although cold gas injection through the base increases the base pressure, the effects of base injection and external compression are not additive.

A new base flow model, for the configuration of Figure 2, is now being developed by Strahle. This model is expected to yield more accurate structure of the base flow region than may be produced by the older Crocco-Lees theory. Furthermore, the model will be capable of treating the case of base injection and entropy layers adjacent to the near wake.

A major problem at the current time is the lack of data against which to test an analytical model. Even data on base pressure and pressure distribution is meager for an axisymmetric case in the absence of injection and burning. This report describes a facility which is designed to test base flow theory at Mach 3.0 so that confidence with which external burning effects can be predicted will be known. Results of preliminary flow evaluation tests and the first series of base flow measurements are also presented.

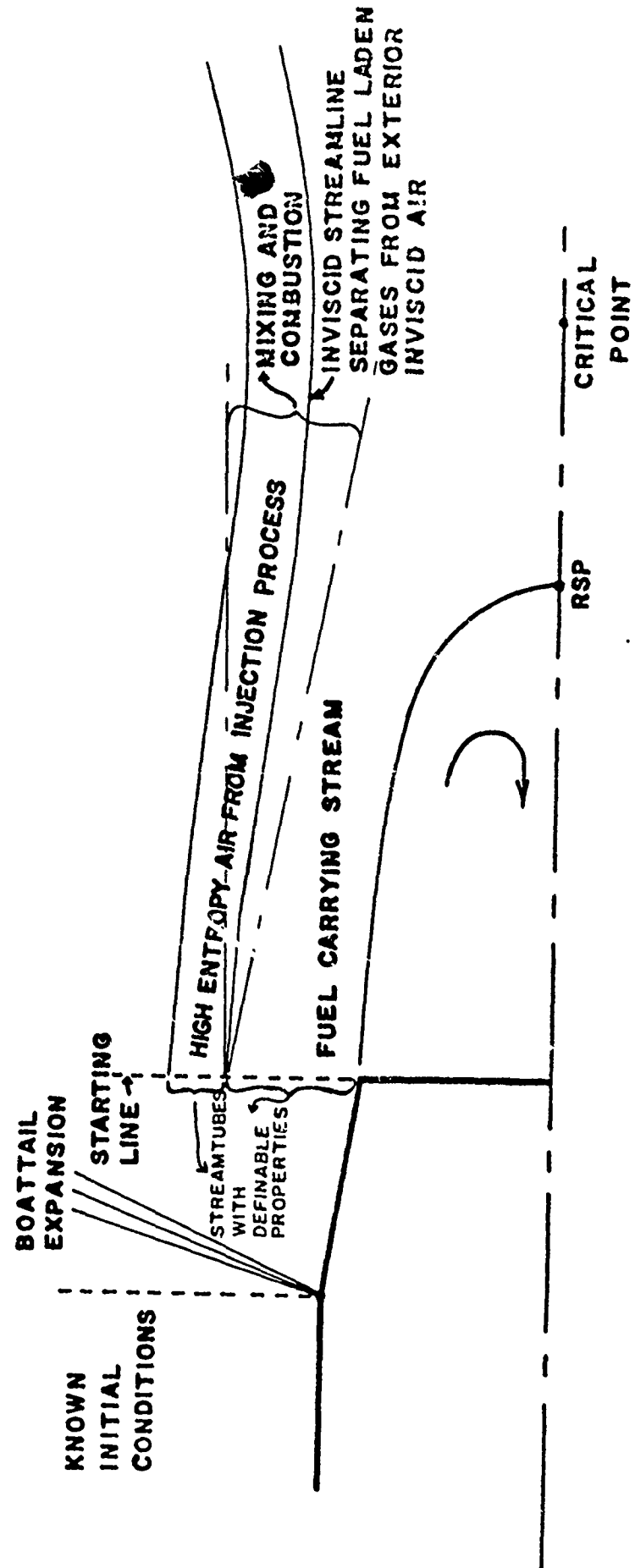


FIGURE 2. FLOW FIELD SCHEMATIC.

## CHAPTER II

## TEST FACILITY

The base flow test facility was designed to simulate the base flow for a projectile at Mach 3 with a fineness ratio of about 6 and Reynolds numbers, based on the diameter, in excess of  $3.0 \times 10^6$ . A relatively large base was selected in order to facilitate experimental accuracy and detailed flow measurements. Furthermore, the facility was designed for the versatility required to expose the base flow to disturbances that simulate those expected with external burning for propulsion. This includes disturbances due to a) axisymmetric pressure waves generated external to the near wake, b) cold gas injection, peripheral to the base in discrete jets, c) base bleed, and d) entropy layers adjacent to the near wake created by axisymmetric and discrete probes ahead of the base plane.

Details of this facility are presented and discussed in the following paragraphs.

Complete Assembly

A schematic of the complete flow system is shown in Figure 3. It is a blow-down system which uses air stored at a maximum pressure of 3000 psia in a cluster of tanks with a total capacity of 500 cu. ft. Air from the storage tanks is reduced to about 400 psia by three remotely controlled, high pressure regulators. The line from these regulators divides into the secondary air supply ducting, which will provide air for either base bleed or radial jets, and the primary tunnel ducting. Each of these ducts has an auxiliary pressure regulator which permits the fine control required for

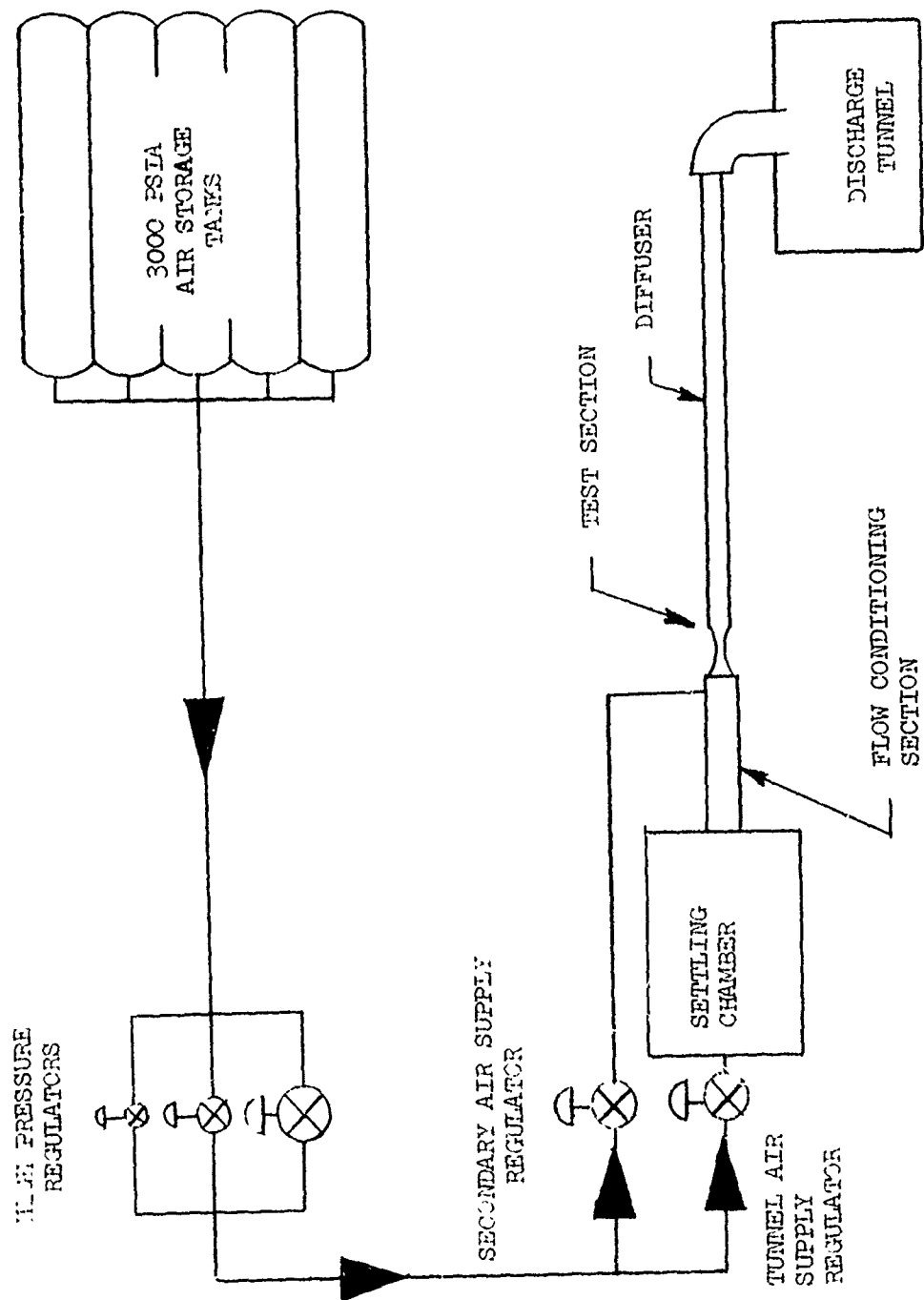


Figure 3. Schematic of the base flow facility flow system.

maintaining accurate test conditions. The combined flows finally dump into a large discharge tunnel. The total run time is from about 3 to in excess of 5 minutes, depending upon the stagnation pressure setting. Secondary air flow, for base bleed and radial jets, will be used later in the program. Therefore, this section of the ducting has not been installed to date.

A more detailed illustration of the test facility is presented in Figure 4. The primary tunnel flow first passes through a settling chamber, consisting of perforated tubes and baffles, which minimizes large scale fluctuations and nonuniformities produced by throttling through the auxiliary pressure regulator. The flow then passes through a final flow conditioning section, consisting of a series of screens and honeycomb, before entering the nozzle and test section. The supersonic flow in the test section is then decelerated in a constant area, shock diffuser before being dumped into the discharge tunnel.

Three spacers, each having an axial length of one base radius and located between the nozzle and external compression section, are illustrated in the schematic of Figure 4. Each of these may be removed to change the location of the external compression section relative to the base.

Photographs of the base-flow test facility are shown in Figure 5. These photographs show the existing configuration and identifies the components from the settling chamber to the diffuser. The probe actuator is remotely stepped radially in increments of 0.001 inch by a stepping motor driving an accurate, no-backlash lead screw. It is manually moved horizontally on two sets of rigid guide rods.

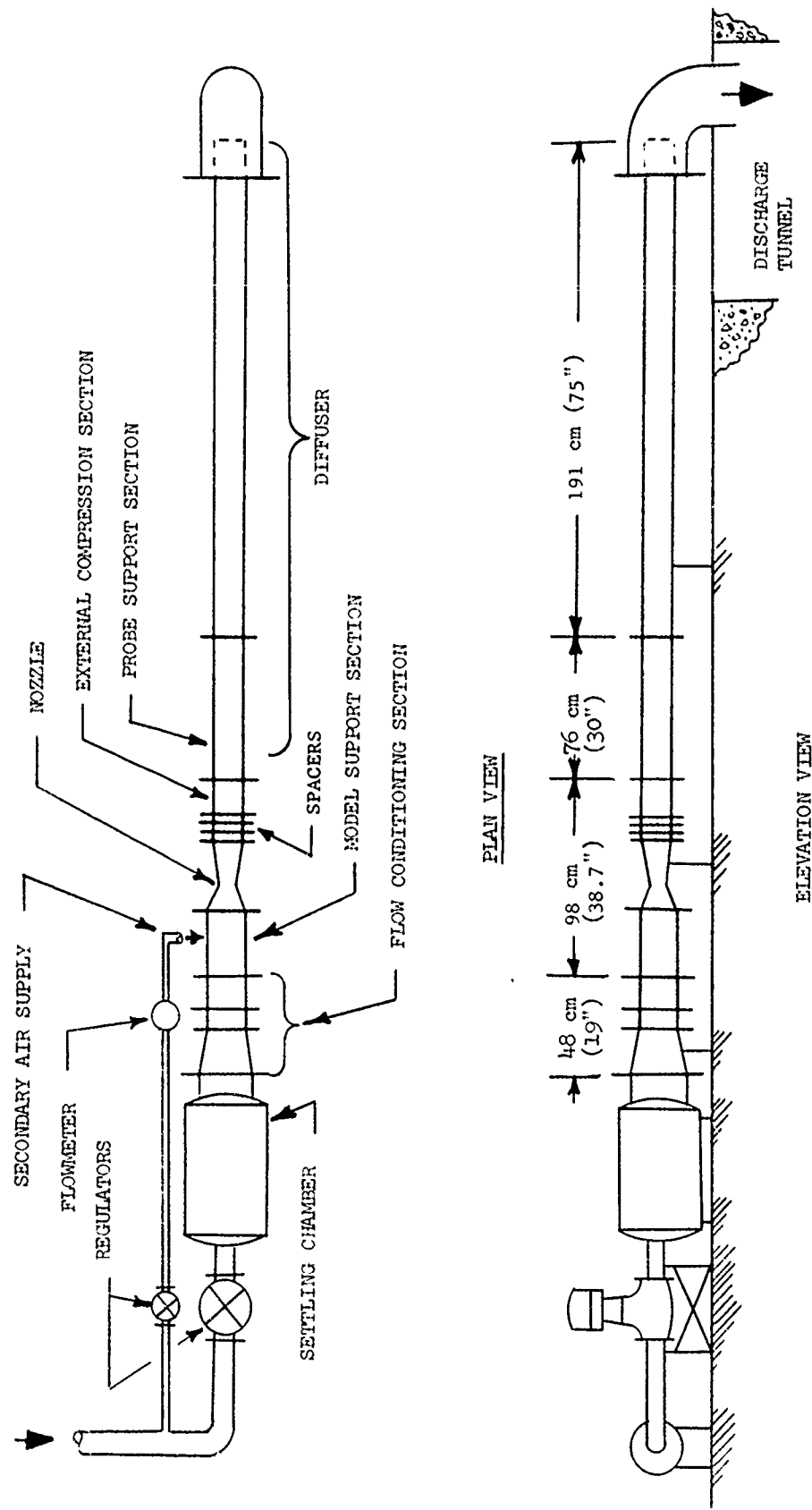


Figure 4. Schematic of the base flow test facility.

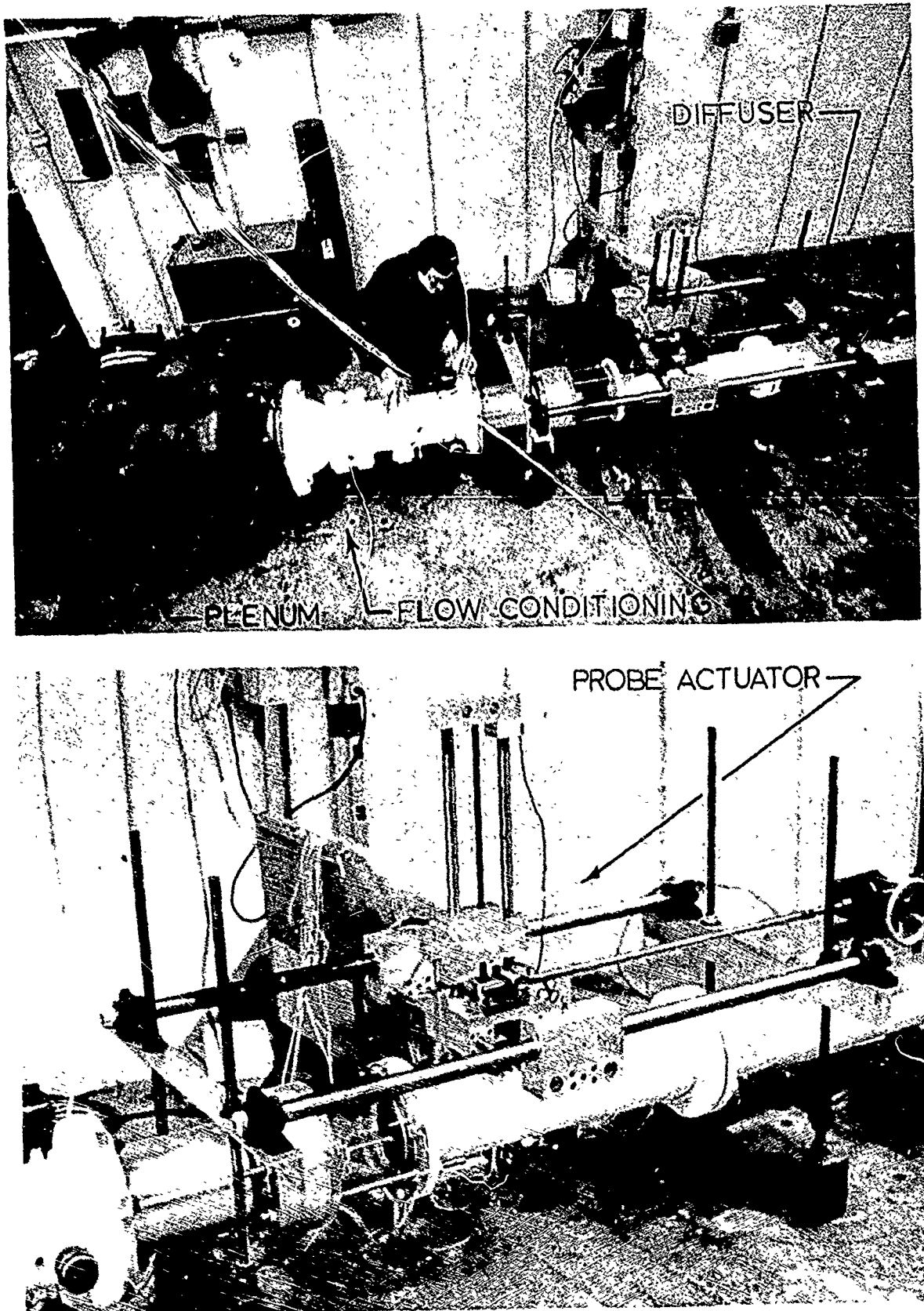


FIGURE 5 BASE FLOW TEST FACILITY

### Flow Conditioning Section

Details of the flow conditioning section are shown in Figure 6. Flow from the settling chamber enters this section through a one-inch thick perforated plate with 1,627 drilled holes 0.07 inches in diameter. The flow through perforations is slightly subcritical and the stagnation pressure ratio across the plate is about 1.5. A one-inch deep honeycomb section, constructed of 0.002 inch thick aluminum with a 0.11 inch mesh, is located immediately downstream of the perforated plate to remove axial components of vorticity generated by unsymmetric coalescence of adjacent jets. The duct is then reduced to the 8-inch diameter employed upstream of the supersonic nozzle. Three 36-mesh stainless steel screens constructed of 0.0065 inch diameter wire are located between flanges in the 8-inch ducting. The screen open-area ratio of 0.59 is in the range of stable flow downstream of the screen.<sup>(20)</sup> The pressure drop coefficient for these three screens is adequate to eliminate significant turbulence and transverse gradients in the longitudinal velocities. An additional honeycomb is located between the last two screens to remove any remaining axial components of vorticity.

### Test Section

The test section of the base-flow facility is shown on Figure 7. This schematic illustrates the model support section, the supersonic nozzle, the centerbody, and the external compression section. The nozzle is designed to expand the flow from a Mach number of 0.07 in the 8-inch-diameter model support section to 3.02 at the nozzle exit. The outer diameter at the nozzle exit was selected to mate with a standard 6-inch diameter pipe. A centerbody diameter of 2.25 inches, before boundary layer corrections, was then selected for the design. This is conservatively less than that for which

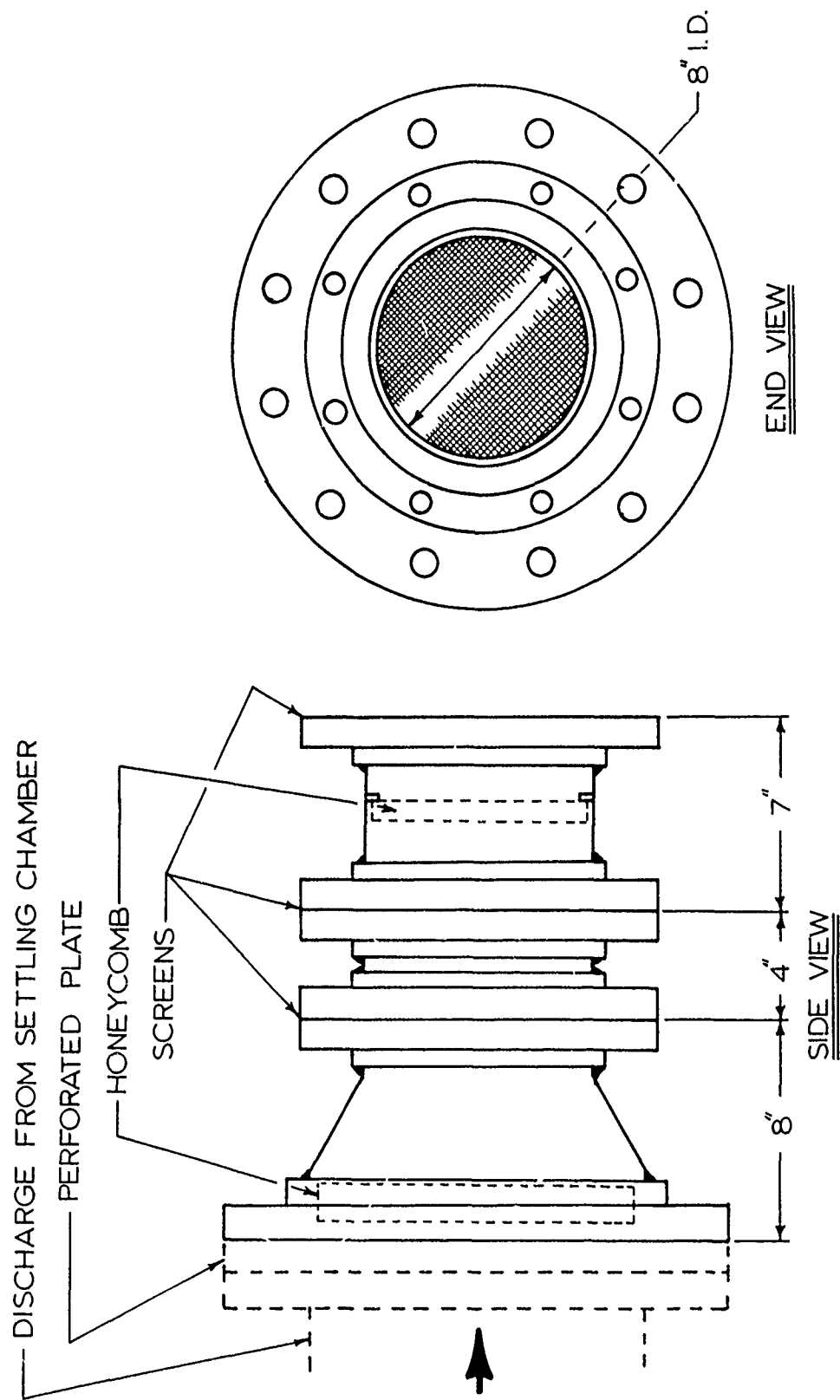


Figure 6. Flow Conditioning Section.

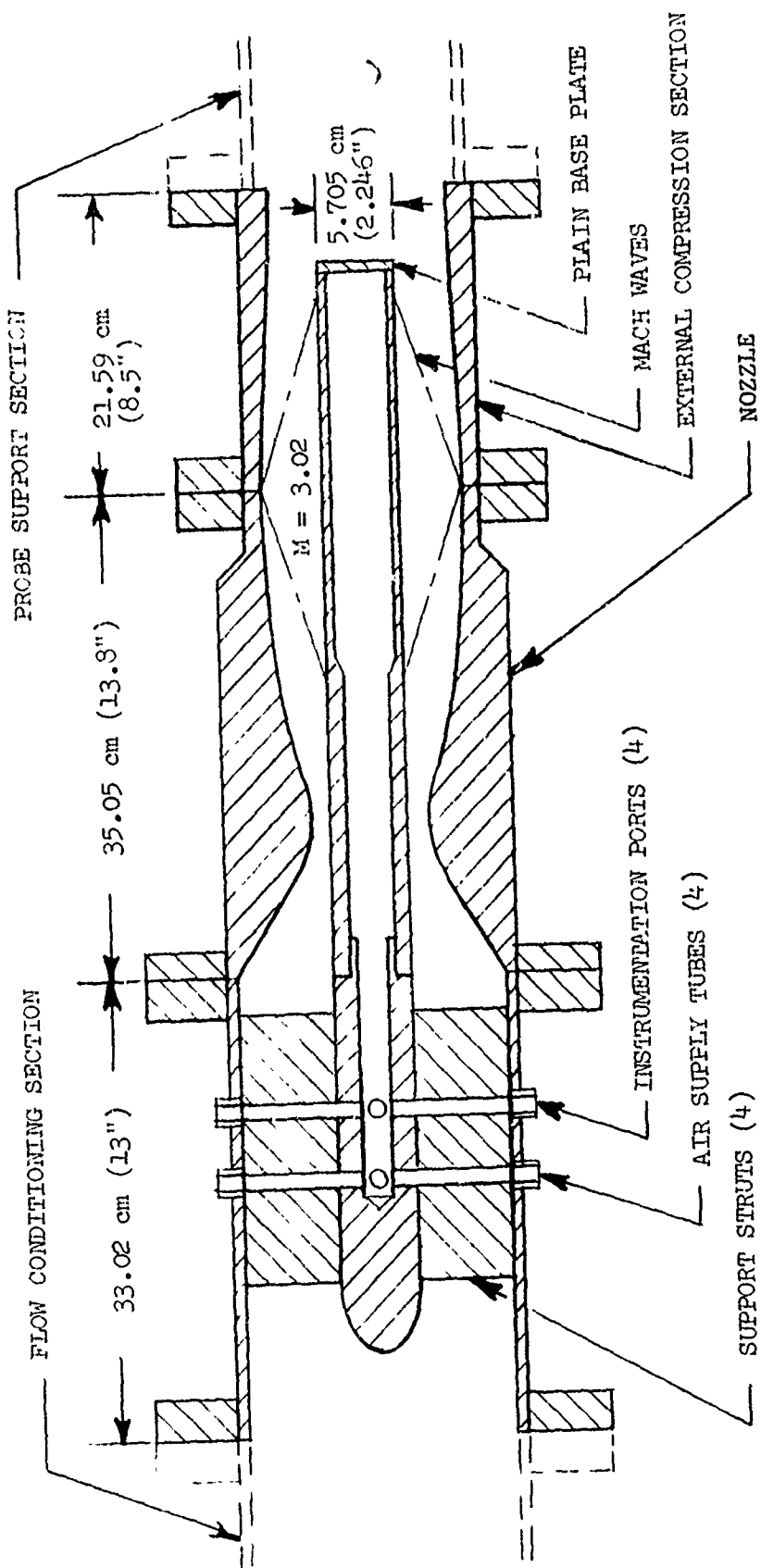


Figure 7. Schematic of the base flow test section.

base expansion waves would reflect from the outer ducting backs to the wake ahead of the critical condition.

The convergence half-angle for the subsonic region of the nozzle is  $30^\circ$ . The throat radius of curvature is five times the throat height. The Mach number distribution in the transonic region was evaluated using an expansion in powers of the reciprocal of the throat radius of curvature following the method of Hall<sup>(21)</sup> modified to incorporate the boundary condition imposed by the constant diameter centerbody. This transonic solution included terms to third order.

The supersonic contour was evaluated using the theory of characteristics starting from the transonic solution at 0.2 throat-heights downstream of the point of minimum area. A very fine characteristic mesh, corresponding to about 125 points on the outer nozzle surface, was used. The outer nozzle contour and the centerbody diameter at the throat are corrected for the boundary layer displacement thickness. The boundary layer development was evaluated using the theory of Cebeci et. al.<sup>(22)</sup> (i.e., a numerical solution of the boundary-layer partial differential equations). Since it was considered to be desirable to maintain a constant diameter centerbody, the centerbody downstream of the throat was not corrected for the slight boundary-layer growth.

The centerbody is constructed in two sections as illustrated in Figure 7. Of particular importance, the long aft section shown in Figure 7 can be removed and replaced by a shorter aft section, thereby reducing the boundary layer thickness on the cylinder ahead of the base by about 60 percent. Only the long aft section has been fabricated to date.

The forward section of the centerbody is supported in the low-speed subsonic region by four streamline struts which provide access to instrumen-

tation in the base model and for the secondary-air supply to be used in later tests. The support section assembly, including the forward section of the centerbody, is shown in Figure 8a. The centerbody forward section is shown in Figure 8b. Each streamline strut contains one secondary-air supply duct and one instrumentation access duct. The mating surfaces of the support pipe, the struts, and the forward section of the centerbody are accurately machined to assure centering. Mating rings on the flanges of the support section and nozzle accurately locate the centerbody in the nozzle.

The external compression section shown in Figure 7 forces the flow to converge toward the axis, simulating the effects of axially symmetric external burning. This particular configuration is designed to approximately eliminate base drag. The design was generated using available experimental data to estimate the required wake convergence and axial pressure gradients and then calculating forward using the method of characteristics to establish the required compression-surface contour. The contour was then slightly adjusted such as to simulate a reasonable and smooth combustion, analytically modeled by one-dimensional, simple, heat addition centered above the wall. The compression surface, the simple heat addition zone, the surface Mach number distribution, and the ratio of the cumulative heat releases,  $\int q dx$ , to the initial enthalpy,  $h$ , are shown in Figure 9. The net heat addition is about three times the initial enthalpy. The external compression section terminates abruptly, forming a base which expands the flow back to the standard 6-inch pipe downstream. This augments the far wake acceleration by imposing an expansion along the wake downstream of the critical point.

The external disturbance section can be moved axially by locating the

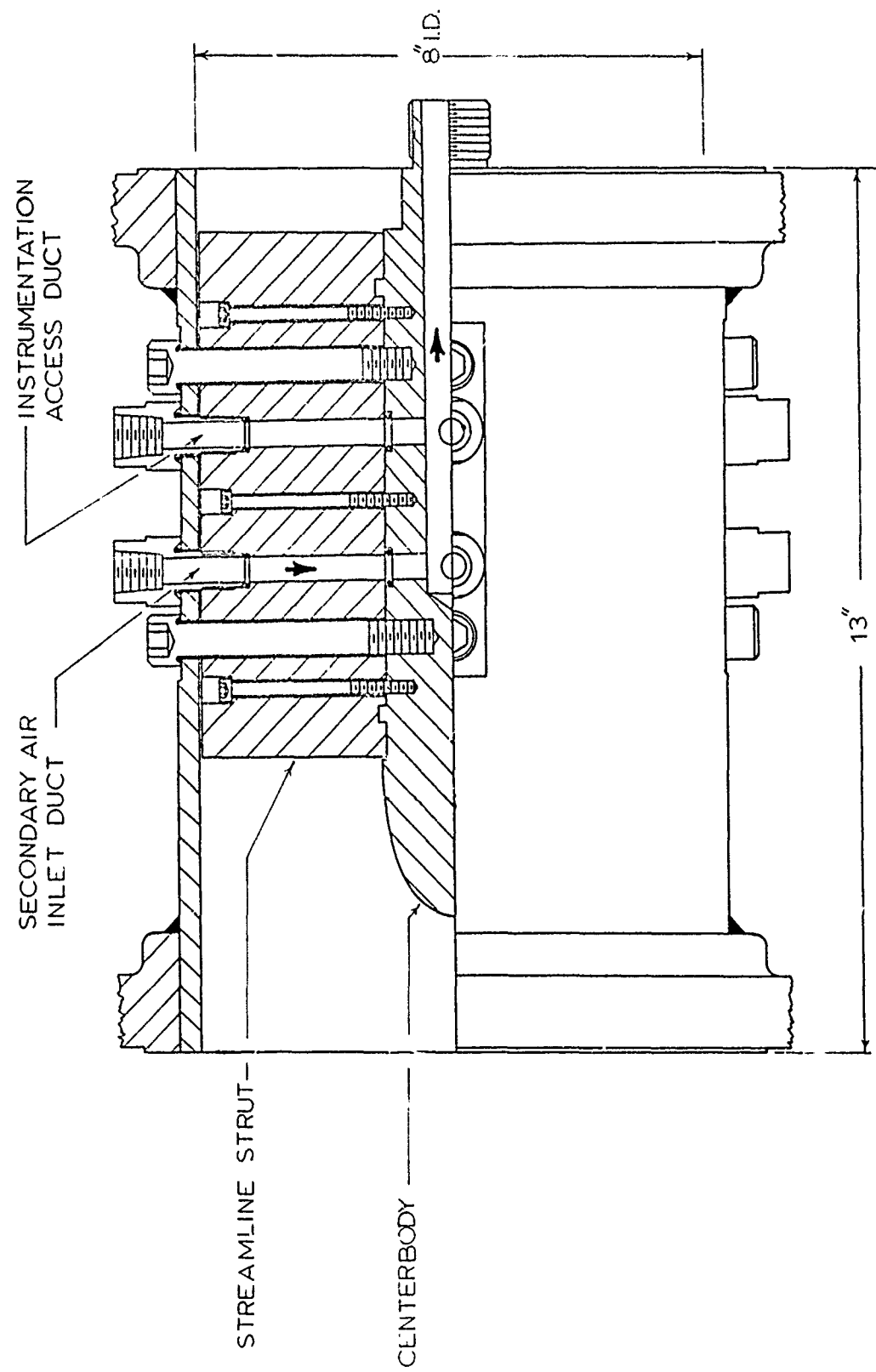


Figure 8a. Centerbody Support Section Assembly.

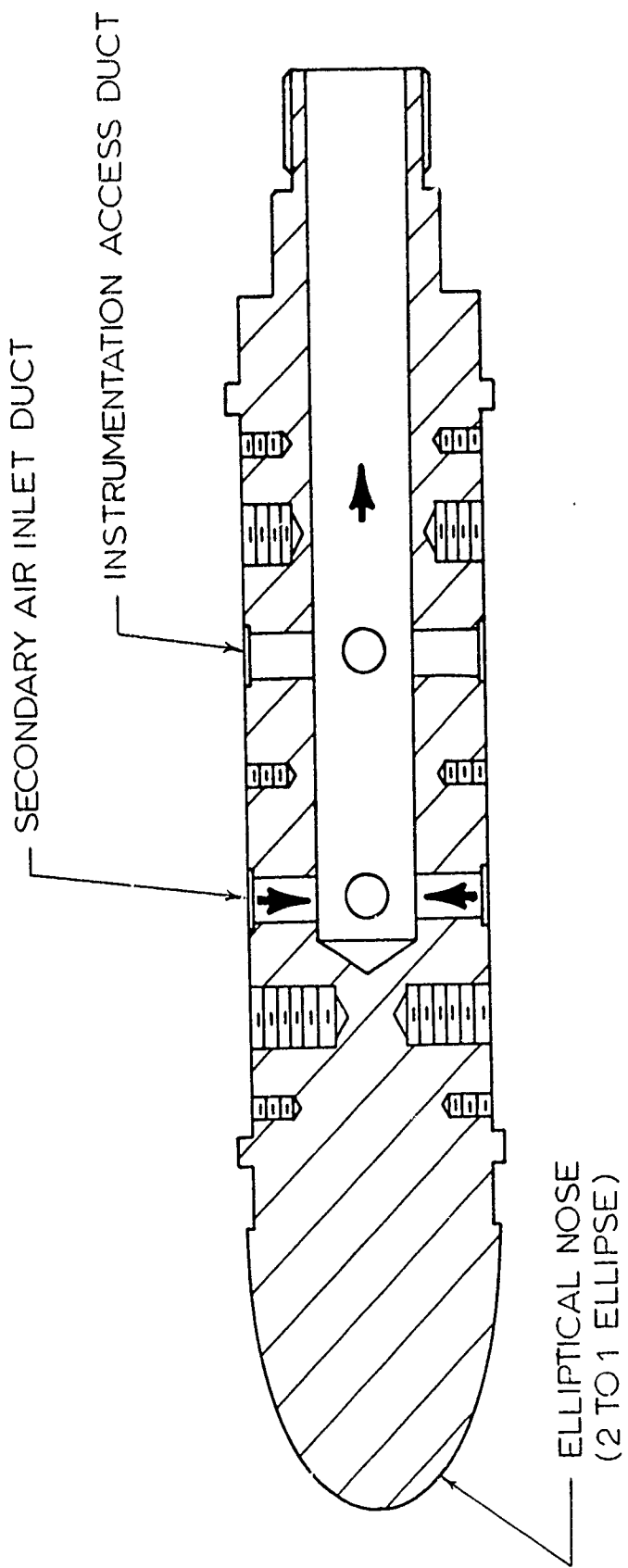


FIGURE 8b. CENTERBODY FORWARD SECTION

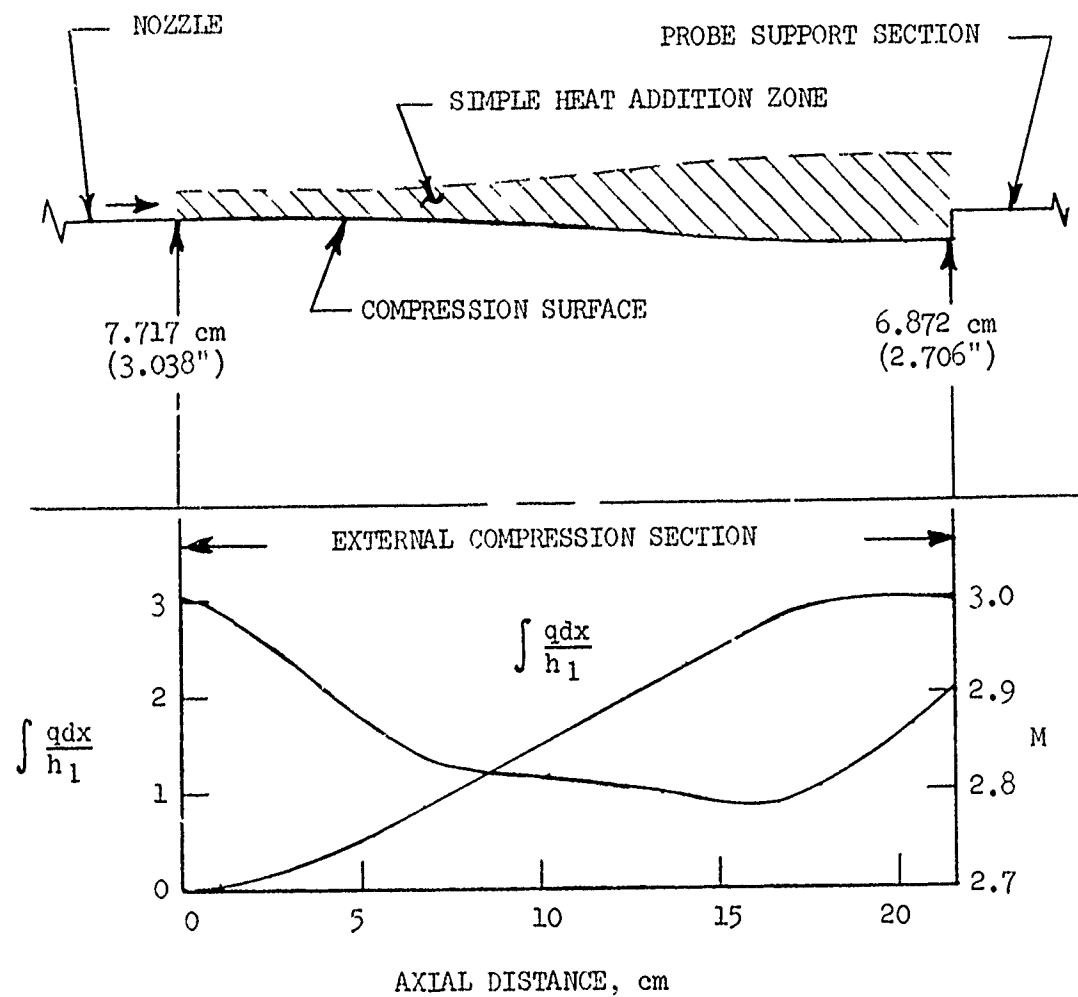


Figure 9. A design of the external compression section and the equivalent cumulative heat release.

constant diameter spacers between the nozzle and the external compression section as indicated in Figure 4. For the configuration shown in Figure 9, the disturbances are initiated one base radius ahead of the base plane. With the three spacers, the disturbances can be moved back in increments of one, two, and three base radii.

The external compression section shown in Figures 7 and 9 has been fabricated but has not been used in tests. Instead, a constant diameter section has been fabricated and used in all tests to date. This configuration has provided basic data without the effects of externally generated disturbances. The next series of tests will use the existing external compression section. Additional external compression sections will then be designed and fabricated for future test series.

A photograph of the test section is shown in Figure 10. This shows the configuration with the constant diameter section downstream of the nozzle. This section is constructed of plexiglas pipe welded to plexiglas flanges. The internal surface is machined and then polished to permit visual monitoring of the base model and probes. All other external compression sections will also be transparent.

#### Diffuser

The flow is decelerated to subsonic speeds in a 6-inch constant diameter shock diffuser. The total diffuser length downstream of the base near wake is 18 duct diameters or 47 base diameters. Such a long diffuser was considered essential if nearly-complete shock diffusion is to be realized because the far wake velocities must first be accelerated by shear stresses before shock deceleration can be initiated. In contrast, fully developed duct flow can be decelerated in a shock diffuser with a length to diameter ratio of about 10. Consequently in the present design nearly half of the

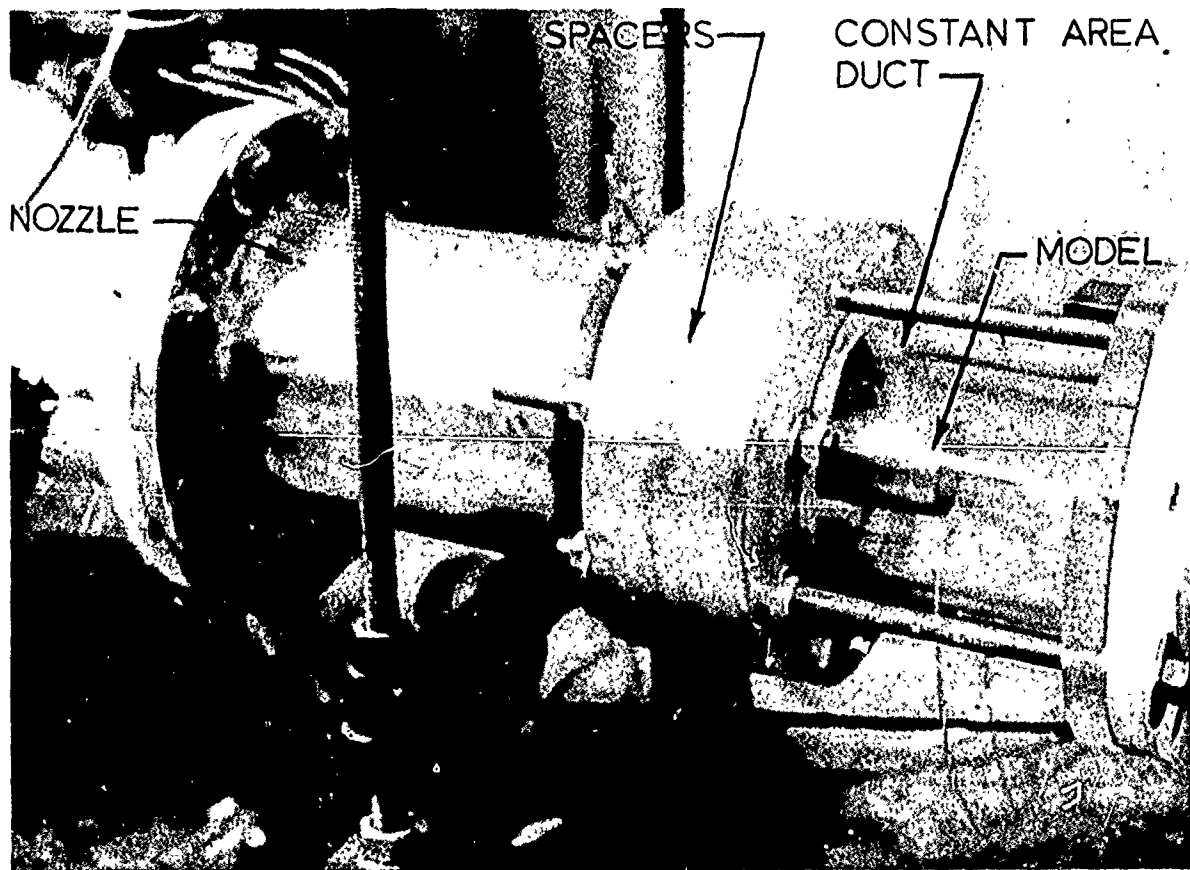


FIGURE 10. TEST SECTION

diffuser length was provided for wake development. It was felt that this would meet the design objective of test section stagnation pressures below 100 psia.

#### Instrumentation

The present test configuration is instrumented with 56 surface static pressure taps; 7 on the base plane, 16 on the cylindrical section of the centerbody, and 33 on the outer ducting from the nozzle exit to the end of the diffuser. Two thermocouples are embeded in the centerbody wall near the base plane and two thermocouples are embeded in the nozzle wall near the exit plane. In addition, a stagnation pressure probe and thermocouple probe are located in the subsonic flow field near the nozzle inlet. Furthermore, the static pressure probe and the pitot probe shown in the photograph of Figure 11 have been used to survey the wake. Both probes are constructed of 0.0625 inch-diameter stainless steel tubing which telescopes into 0.125 and 0.25 inch-diameter tubes for structural support. Long sections of the smaller diameter tubing are used to minimize probe disturbances in the near wake. The 0.0625 inch diameter section of the pitot probe is 3.5 inches long. The four static taps in the static pressure probe are located 4.5 inches from the 0.125 inch diameter tubes. In addition, this 0.0625 inch section of tubing extends 6.5 inches forward of the static taps. This extension threads through a hole in the base plate which provides a secondary support for the probe.

The nozzle-inlet stagnation pressure is measured by a 0-150 psia strain-gage pressure transducer. All other pressures are measured by two 1000 mm Hg, Barocel Electronic Manometers manufactured by Datametric Corporation. These units use highly stable and linear, variable-capacity transducers with

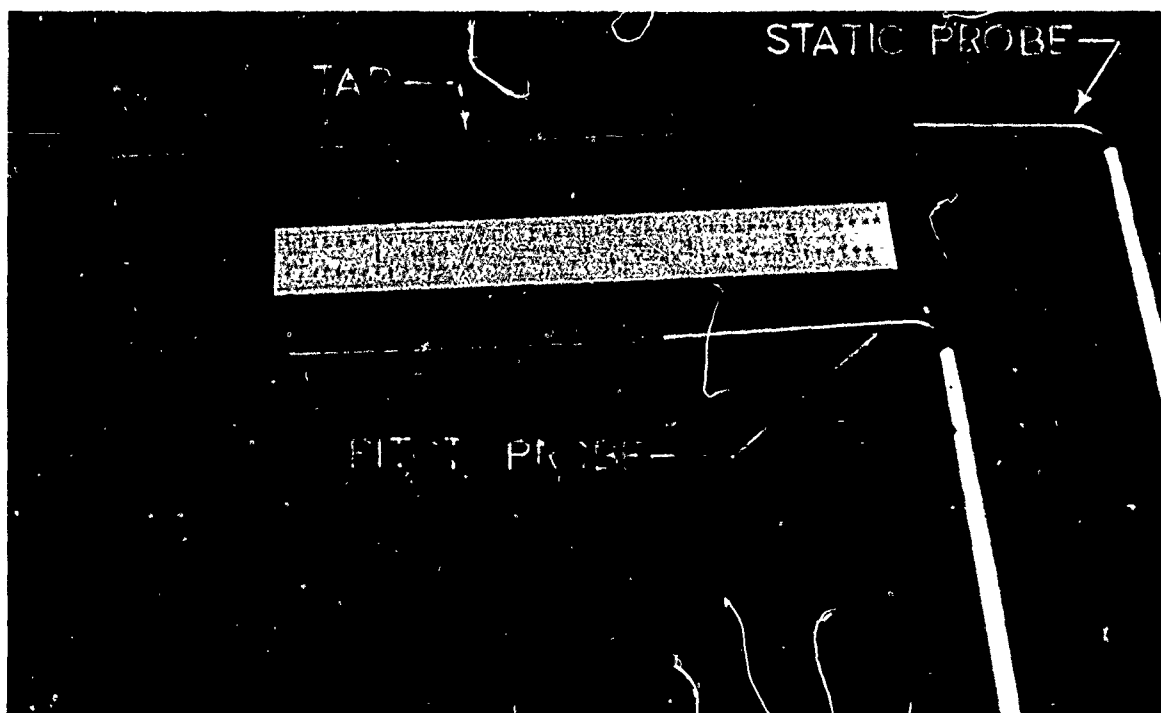
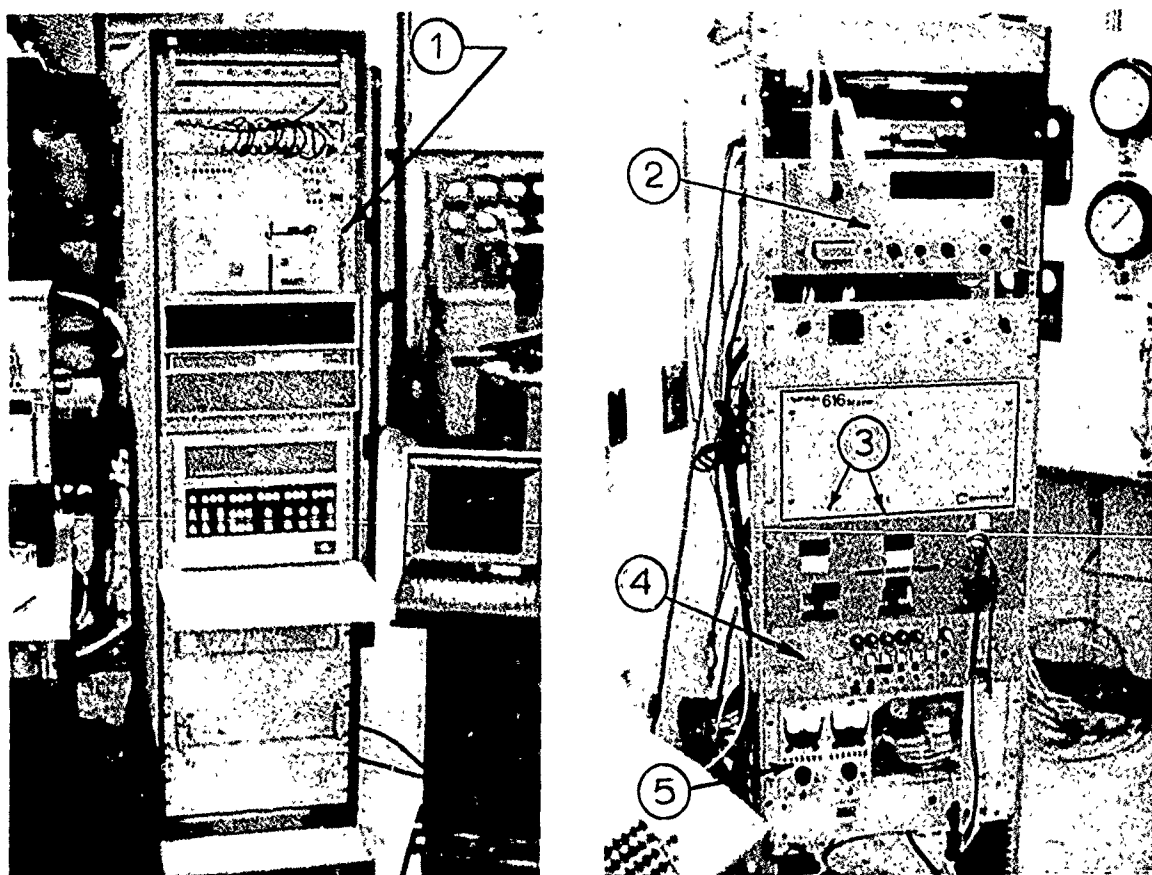


FIGURE 11. STATIC AND PITOT PROBES

automatic ranging output amplification from 1 to 1000. Two 48 channel Scanivalve components are used for rapidly switching the pressures to the two Barocel transducers.

The facility is set up for manual operation during system check-out or for programmed operation, using a computer-based data acquisition system, during the short-duration test runs. The data acquisition system is shown in the photographs of Figure 12. This system uses a Hewlett Packard HP2100A computer with 16K of core storage. The computer is interfaced with a HP2752A teletype for operational control and data output, a high speed tape reader for program inputs, a HP2401C low-level, integrating, digital voltmeter for reading all input voltage data, a 30 channel scanner for connecting the various data channels to the voltmeter, and a 16 contact relay card for actuating the probe drive and scanivalve solenoids. A schematic of the system hook-up is presented in Figure 13.

The use of the high-speed data acquisition both increases the amount and enhances the quality of the data obtained during each short-duration test. During the test the pressure data are normalized by the instantaneous upstream stagnation pressure to minimize the effects of drifts in test conditions and then stored for later retrieval. Output is generally arranged for a convenient display for rapid assessment of the results. Typical examples of data output are presented in Figure 14. Figures 14a and 14b show the data output for a Reynolds number test consisting of four runs; each run corresponding to a given initial stagnation pressure setting. The normalized surface static pressures are displayed in Figure 14a. The stagnation pressures used to normalize the static pressures are displayed in Figure 14b. The stagnation pressure is measured once for every two static pressure measurements (the static pressure measurements being in the order



1. COMPUTER
2. INTEGRATING DIGITAL VOLTMETER
3. SCANIVALE POSITION INDICATORS
4. SCANIVALE CONTROLLERS
5. BAROCEL SIGNAL CONDITIONERS

FIGURE 12. DATA ACQUISITION SYSTEM

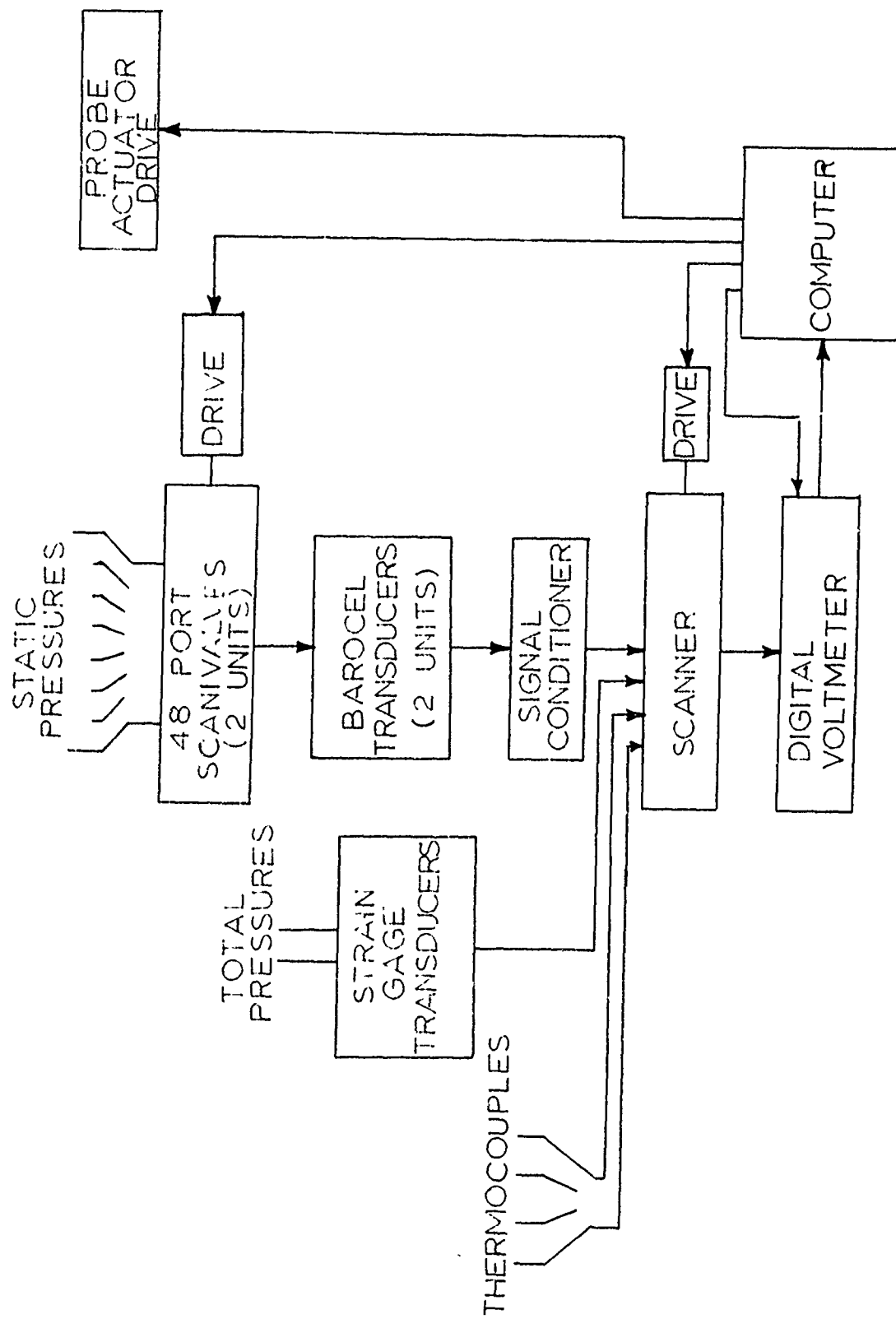


FIGURE 13. SCHEMATIC OF DATA ACQUISITION SYSTEM

	P(J,1)/P01	P(J,2)/P01	P(J,3)/P01	P(J,4)/P01
1	1.32914E-02	1.32914E-02	1.32914E-02	1.32521E-02
2	1.37113E-02	1.35137E-02	1.34450E-02	1.37570E-02
3	1.42777E-02	1.42679E-02	1.41745E-02	1.43279E-02
4	1.45475E-02	1.43182E-02	1.41299E-02	1.43070E-02
5	1.47421E-02	1.44331E-02	1.47632E-02	1.49931E-02
6	1.47774E-02	1.47710E-02	1.47423E-02	1.48481E-02
7	1.49193E-02	1.48142E-02	1.47174E-02	1.49150E-02
8	1.49921E-02	1.49998E-02	1.48795E-02	1.48400E-02
9	1.51305E-02	1.48775E-02	1.48765E-02	1.48820E-02
10	1.51942E-02	1.47472E-02	1.47099E-02	1.49484E-02
11	1.52774E-02	1.45649E-02	1.45302E-02	1.45477E-02
12	1.53193E-02	1.43142E-02	1.42174E-02	1.42267E-02
13	1.53924E-02	1.40998E-02	1.40753E-02	1.40401E-02
14	1.54475E-02	1.38757E-02	1.38765E-02	1.38703E-02
15	1.55302E-02	1.37429E-02	1.37357E-02	1.37803E-02
16	1.55477E-02	1.36159E-02	1.36144E-02	1.36191E-02
17	1.55547E-02	1.35039E-02	1.35745E-02	1.35510E-02
18	1.55571E-02	1.34674E-02	1.34629E-02	1.34629E-02
19	1.55644E-02	1.34024E-02	1.34024E-02	1.34439E-02
20	1.55674E-02	1.33769E-02	1.33769E-02	1.34493E-02
21	1.55702E-02	1.33129E-02	1.33129E-02	1.34673E-02
22	1.55730E-02	1.32632E-02	1.32632E-02	1.34659E-02
23	1.55757E-02	1.32269E-02	1.32269E-02	1.34673E-02
24	1.55785E-02	1.31973E-02	1.31973E-02	1.34659E-02
25	1.55812E-02	1.31451E-02	1.31451E-02	1.34681E-02
26	1.55841E-02	1.30909E-02	1.30941E-02	1.34700E-02
27	1.55864E-02	1.30341E-02	1.30341E-02	1.34710E-02
28	1.55882E-02	1.29779E-02	1.29739E-02	1.34723E-02
29	1.55901E-02	1.29210E-02	1.29171E-02	1.34733E-02
30	1.55918E-02	1.28643E-02	1.28604E-02	1.34744E-02
31	1.55935E-02	1.28075E-02	1.28036E-02	1.34755E-02
32	1.55952E-02	1.27508E-02	1.27469E-02	1.34766E-02
33	1.55969E-02	1.26941E-02	1.26891E-02	1.34777E-02
34	1.55986E-02	1.26374E-02	1.26335E-02	1.34788E-02
35	1.55993E-02	1.25797E-02	1.25758E-02	1.34800E-02
36	1.56009E-02	1.25220E-02	1.25181E-02	1.34811E-02
37	1.56025E-02	1.24643E-02	1.24604E-02	1.34822E-02
38	1.56041E-02	1.24066E-02	1.24027E-02	1.34834E-02
39	1.56057E-02	1.23489E-02	1.23450E-02	1.34844E-02
40	1.56073E-02	1.22912E-02	1.22873E-02	1.34855E-02
41	1.56089E-02	1.22335E-02	1.22296E-02	1.34866E-02
42	1.56105E-02	1.21758E-02	1.21719E-02	1.34877E-02
43	1.56121E-02	1.21181E-02	1.21142E-02	1.34888E-02
44	1.56137E-02	1.20604E-02	1.20565E-02	1.34899E-02
45	1.56153E-02	1.19927E-02	1.19888E-02	1.34910E-02
46	1.56169E-02	1.19350E-02	1.19311E-02	1.34921E-02
47	1.56185E-02	1.18773E-02	1.18734E-02	1.34932E-02
48	1.56201E-02	1.18206E-02	1.18167E-02	1.34943E-02
49	1.56217E-02	1.17630E-02	1.17591E-02	1.34954E-02
50	1.56233E-02	1.17053E-02	1.17014E-02	1.34965E-02
51	1.56249E-02	1.16476E-02	1.16437E-02	1.34976E-02
52	1.56265E-02	1.15899E-02	1.15860E-02	1.34987E-02
53	1.56281E-02	1.15322E-02	1.15283E-02	1.34998E-02
54	1.56297E-02	1.14745E-02	1.14706E-02	1.35009E-02
55	1.56313E-02	1.14168E-02	1.14129E-02	1.35020E-02
56	1.56329E-02	1.13591E-02	1.13552E-02	1.35031E-02
57	1.56345E-02	1.13014E-02	1.12975E-02	1.35042E-02
58	1.56361E-02	1.12437E-02	1.12398E-02	1.35053E-02
59	1.56377E-02	1.11860E-02	1.11821E-02	1.35064E-02
60	1.56393E-02	1.11283E-02	1.11244E-02	1.35075E-02
61	1.56409E-02	1.10706E-02	1.10667E-02	1.35086E-02
62	1.56425E-02	1.10129E-02	1.10089E-02	1.35097E-02
63	1.56441E-02	1.09552E-02	1.09513E-02	1.35108E-02
64	1.56457E-02	1.08975E-02	1.08936E-02	1.35119E-02
65	1.56473E-02	1.08398E-02	1.08359E-02	1.35131E-02
66	1.56489E-02	1.07821E-02	1.07782E-02	1.35142E-02
67	1.56505E-02	1.07244E-02	1.07205E-02	1.35153E-02
68	1.56521E-02	1.06667E-02	1.06628E-02	1.35164E-02
69	1.56537E-02	1.06090E-02	1.06051E-02	1.35175E-02
70	1.56553E-02	1.05513E-02	1.05474E-02	1.35186E-02
71	1.56569E-02	1.04936E-02	1.04897E-02	1.35197E-02
72	1.56585E-02	1.04359E-02	1.04320E-02	1.35208E-02
73	1.56601E-02	1.03782E-02	1.03743E-02	1.35219E-02
74	1.56617E-02	1.03205E-02	1.03166E-02	1.35230E-02
75	1.56633E-02	1.02628E-02	1.02589E-02	1.35241E-02
76	1.56649E-02	1.02051E-02	1.01999E-02	1.35252E-02
77	1.56665E-02	1.01474E-02	1.01435E-02	1.35263E-02
78	1.56681E-02	1.00897E-02	1.00858E-02	1.35274E-02
79	1.56697E-02	1.00320E-02	1.00281E-02	1.35285E-02
80	1.56713E-02	1.00143E-02	1.00104E-02	1.35296E-02
81	1.56729E-02	1.00066E-02	1.00027E-02	1.35307E-02
82	1.56745E-02	1.00000E-02	1.00000E-02	1.35318E-02
83	1.56761E-02	1.00000E-02	1.00000E-02	1.35329E-02
84	1.56777E-02	1.00000E-02	1.00000E-02	1.35340E-02
85	1.56793E-02	1.00000E-02	1.00000E-02	1.35351E-02
86	1.56809E-02	1.00000E-02	1.00000E-02	1.35362E-02
87	1.56825E-02	1.00000E-02	1.00000E-02	1.35373E-02
88	1.56841E-02	1.00000E-02	1.00000E-02	1.35384E-02
89	1.56857E-02	1.00000E-02	1.00000E-02	1.35395E-02
90	1.56873E-02	1.00000E-02	1.00000E-02	1.35406E-02
91	1.56889E-02	1.00000E-02	1.00000E-02	1.35417E-02
92	1.56905E-02	1.00000E-02	1.00000E-02	1.35428E-02
93	1.56921E-02	1.00000E-02	1.00000E-02	1.35439E-02
94	1.56937E-02	1.00000E-02	1.00000E-02	1.35450E-02
95	1.56953E-02	1.00000E-02	1.00000E-02	1.35461E-02
96	1.56969E-02	1.00000E-02	1.00000E-02	1.35472E-02
97	1.56985E-02	1.00000E-02	1.00000E-02	1.35483E-02
98	1.56997E-02	1.00000E-02	1.00000E-02	1.35494E-02
99	1.57013E-02	1.00000E-02	1.00000E-02	1.35505E-02
100	1.57029E-02	1.00000E-02	1.00000E-02	1.35516E-02
101	1.57045E-02	1.00000E-02	1.00000E-02	1.35527E-02
102	1.57061E-02	1.00000E-02	1.00000E-02	1.35538E-02
103	1.57077E-02	1.00000E-02	1.00000E-02	1.35549E-02
104	1.57093E-02	1.00000E-02	1.00000E-02	1.35560E-02
105	1.57109E-02	1.00000E-02	1.00000E-02	1.35571E-02
106	1.57125E-02	1.00000E-02	1.00000E-02	1.35582E-02
107	1.57141E-02	1.00000E-02	1.00000E-02	1.35593E-02
108	1.57157E-02	1.00000E-02	1.00000E-02	1.35604E-02
109	1.57173E-02	1.00000E-02	1.00000E-02	1.35615E-02
110	1.57189E-02	1.00000E-02	1.00000E-02	1.35626E-02
111	1.57205E-02	1.00000E-02	1.00000E-02	1.35637E-02
112	1.57221E-02	1.00000E-02	1.00000E-02	1.35648E-02
113	1.57237E-02	1.00000E-02	1.00000E-02	1.35659E-02
114	1.57253E-02	1.00000E-02	1.00000E-02	1.35670E-02
115	1.57269E-02	1.00000E-02	1.00000E-02	1.35681E-02
116	1.57285E-02	1.00000E-02	1.00000E-02	1.35692E-02
117	1.57301E-02	1.00000E-02	1.00000E-02	1.35703E-02
118	1.57317E-02	1.00000E-02	1.00000E-02	1.35714E-02
119	1.57333E-02	1.00000E-02	1.00000E-02	1.35725E-02
120	1.57349E-02	1.00000E-02	1.00000E-02	1.35736E-02
121	1.57365E-02	1.00000E-02	1.00000E-02	1.35747E-02
122	1.57381E-02	1.00000E-02	1.00000E-02	1.35758E-02
123	1.57397E-02	1.00000E-02	1.00000E-02	1.35769E-02
124	1.57413E-02	1.00000E-02	1.00000E-02	1.35780E-02
125	1.57429E-02	1.00000E-02	1.00000E-02	1.35791E-02
126	1.57445E-02	1.00000E-02	1.00000E-02	1.35802E-02
127	1.57461E-02	1.00000E-02	1.00000E-02	1.35813E-02
128	1.57477E-02	1.00000E-02	1.00000E-02	1.35824E-02
129	1.57493E-02	1.00000E-02	1.00000E-02	1.35835E-02
130	1.57509E-02	1.00000E-02	1.00000E-02	1.35846E-02
131	1.57525E-02	1.00000E-02	1.00000E-02	1.35857E-02
132	1.57541E-02	1.00000E-02	1.00000E-02	1.35868E-02
133	1.57557E-02	1.00000E-02	1.00000E-02	1.35879E-02
134	1.57573E-02	1.00000E-02	1.00000E-02	1.35890E-02
135	1.57589E-02	1.00000E-02	1.00000E-02	1.35901E-02
136	1.57605E-02	1.00000E-02	1.00000E-02	1.35912E-02
137	1.57621E-02	1.00000E-02	1.00000E-02	1.35923E-02
138	1.57637E-02	1.00000E-02	1.00000E-02	1.35934E-02
139	1.57653E-02	1.00000E-02	1.00000E-02	1.35945E-02
140	1.57669E-02	1.00000E-02	1.00000E-02	1.35956E-02
141	1.57685E-02	1.00000E-02	1.00000E-02	1.35967E-02
142	1.57701E-02	1.00000E-02	1.00000E-02	1.35978E-02
143	1.57717E-02	1.00000E-02	1.00000E-02	1.35989E-02
144	1.57733E-02	1.00000E-02	1.00000E-02	1.35990E-02

J STATIC PRESSURE TAP INDEX

K RUN INDEX

P(J,K) STATIC PRESSURE ARRAY

P01 STAGNATION PRESSURE

**COPY AVAILABLE TO DDC DOES NOT  
PERMIT FULLY LEGIBLE PRODUCTION**

I	P01(1)	P01(2)	P01(3)	P01(4)
1	4066.34	5009.	7531.6	6449.52
2	4072.39	5059.79	7554.17	6416.31
3	4061.2	5009.51	7523.32	6440.12
4	4061.0	5030.2	7492.11	6435.12
5	4042.44	5027.91	7461.27	6423.12
6	4053.67	4999.6	7478.19	6410.43
7	4049.44	5054.65	7454.49	6411.91
8	4032.22	4977.54	7448.85	6406.27
9	4042.44	5030.2	7446.22	6399.39
10	4025.47	4995.84	7426.28	6402.5
11	4040.51	4978.01	7430.45	6381.82
12	4010.32	5025.93	7401.09	6334.1
13	4007.35	4956.35	7419.89	6363.01
14	4010.93	4998.22	7391.68	6372.41
15	4007.35	4995.84	7377.38	6354.25
16	3992.14	4928.14	7375.5	6352.37
17	4017.94	4999.2	7372.52	6341.04
18	4001.42	4966.25	7362.34	6342.97
19	4002.2	4910.23	7352.19	6335.44
20	3995.38	4994.56	7331.51	6331.74
21	3992.02	4932.4	7350.31	6321.64
22	3992.5	4916.47	7353.48	6310.36

I	T0(K)	T1(K)	T2(K)
1	55.021	63.0693	73.4481
2	35.0730	29.6113	63.0767
3	16.2476	-18277	49.0168
4	-3.17974	-26.2115	30.0045

I STAGNATION PRESSURE MEASUREMENT INDEX  
 K RUN INDEX  
 P01(K) STAGNATION PRESSURE, mmHG  
 TO(K) STAGNATION TEMPERATURE, °F  
 T1(K) CENTERBODY WALL TEMPERATURE, °F  
 T2(K) NOZZLE WALL TEMPERATURE, °F  
 b) STAGNATION PRESSURE, STAGNATION TEMPERATURE, AND WALL TEMPERATURE DATA

FIGURE 14. CONTINUED.

COPY AVAILABLE TO DDC DOES NOT  
PERMIT FULLY LICENSED PRODUCTION

	(1) P1	P2	P3	T1
125	1.29970E-02	1.39083E-02	4134.96	48.559
150	1.29800E-02	1.39075E-02	4116.56	44.5443
175	1.42491E-02	1.40800E-02	4074.77	41.9725
200	1.60763E-02	1.40001E-02	4076.65	33.723
225	1.79374E-02	1.41203E-02	4015.78	35.5846
250	2.00501E-02	1.41771E-02	4083.10	31.9523
275	2.24503E-02	1.44194E-02	3988.66	26.9209
300	2.46151E-02	1.43269E-02	3979.21	21.8232
325	2.63504E-02	1.43240E-02	3966.20	19.0076
350	2.80006E-02	1.40934E-02	3977.37	16.2476
375	3.04579E-02	1.40279E-02	3974.84	14.3784
400	3.12501E-02	1.41908E-02	3909.45	10.6236
425	3.17125E-02	1.42843E-02	3935.6	8.73721
450	3.21155E-02	1.45099E-02	3915.3	5.94606
475	3.37436E-02	1.42542E-02	3922.43	3.59342
500	3.41346E-02	1.46271E-02	3856.6	1.66698
525	3.43950E-02	1.45717E-02	3843.83	.601072
550	3.43377E-02	1.46500E-02	3822.75	-1.68127
575	3.35720E-02	1.44127E-02	3858.48	-3.17570
600	3.40000E-02	1.43231E-02	3854.72	-4.13861
625	3.41545E-02	1.46822E-02	3808.09	-6.06879
				-7.94699

PROBE P      STATIC PROBE PRESSURE  
 P(1)      A BASE STATIC PRESSURE  
 X      AXIAL DISTANCE FROM BASE,  $\times 10^2$  INCHES

c) WAKE AXIAL STATIC PRESSURE SURVEY

FIGURE 14. CONTINUED.

of the tap numbers) and then this stagnation pressure is used to normalize the two static pressures. This sequence is continued until all static pressures are measured. Figure 14b also lists the temperatures which were measured at the beginning of each run. The total test time for the data of Figures 14a and 14b was less than 3 minutes.

Figure 14c displays part of the data taken during the static pressure survey along the axis. The stagnation pressure and a base static pressure are measured each time the probe static pressure is measured. The stagnation pressure is then used to normalize the other two pressures.

## CHAPTER III

## RESULTS OF FLOW AND DATA EVALUATION TESTS

Preliminary tests were made to evaluate the quality of the flow field, the accuracy and repeatability of test data, and limits of test conditions prior to starting detailed base flow tests. The results of these evaluation studies are presented and discussed in this chapter.

Nozzle Inlet Flow

Velocity distributions along the horizontal and vertical lines through the center of the 8-inch duct upstream of the model support section are shown in Figure 15. The local velocity,  $u$ , is normalized by the numerical average of all velocities,  $\bar{u}$ . The maximum deviation from the average velocity is less than one percent. Since the mean flow Mach number in this section of ducting is only 0.035 the differences between the stagnation pressures of the nozzle inlet streamlines is negligible in comparison with the test-section dynamic head. It may be concluded that the settling chamber, the perforated plate, and the screens and honeycombs in the flow conditioning sections have eliminated the flow non-uniformities created by the large pressure drops through the control valves.

The nozzle inlet stagnation pressure decreases slowly with time after the upstream control valves have been adjusted for a particular pressure setting. A typical variation is illustrated in Figure 16 where the ratios of the stagnation pressure,  $P_o$ , to the initial stagnation pressure,  $P_{o_1}$ , are plotted against test time. In this case, the stagnation pressure decreases by about four percent in one minute. A cyclic variation, perhaps due to long

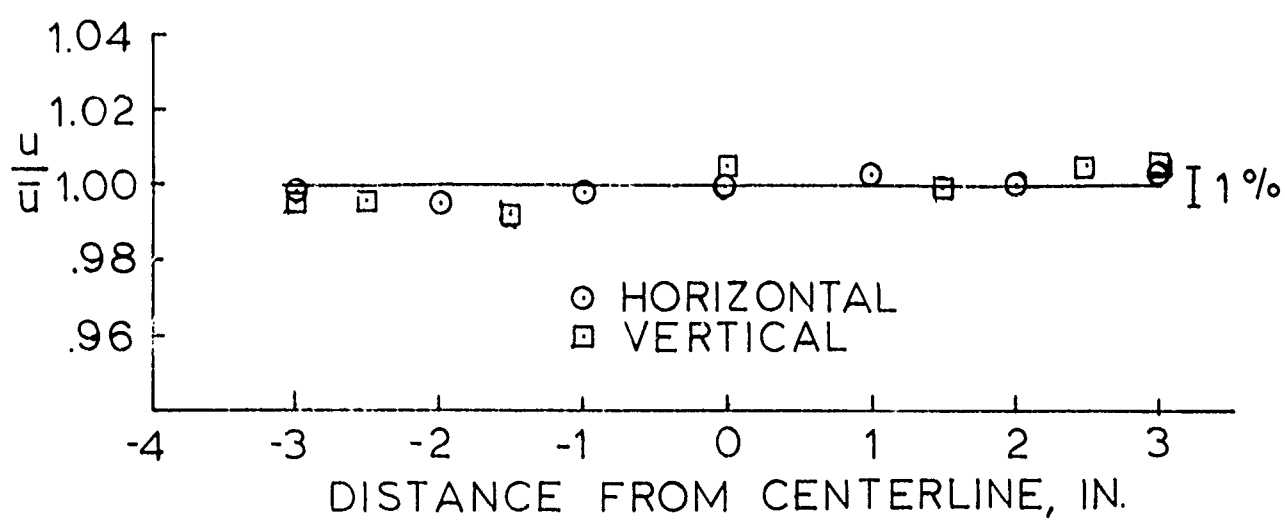


FIGURE 15. VELOCITY DISTRIBUTIONS AT TEST SECTION INLET

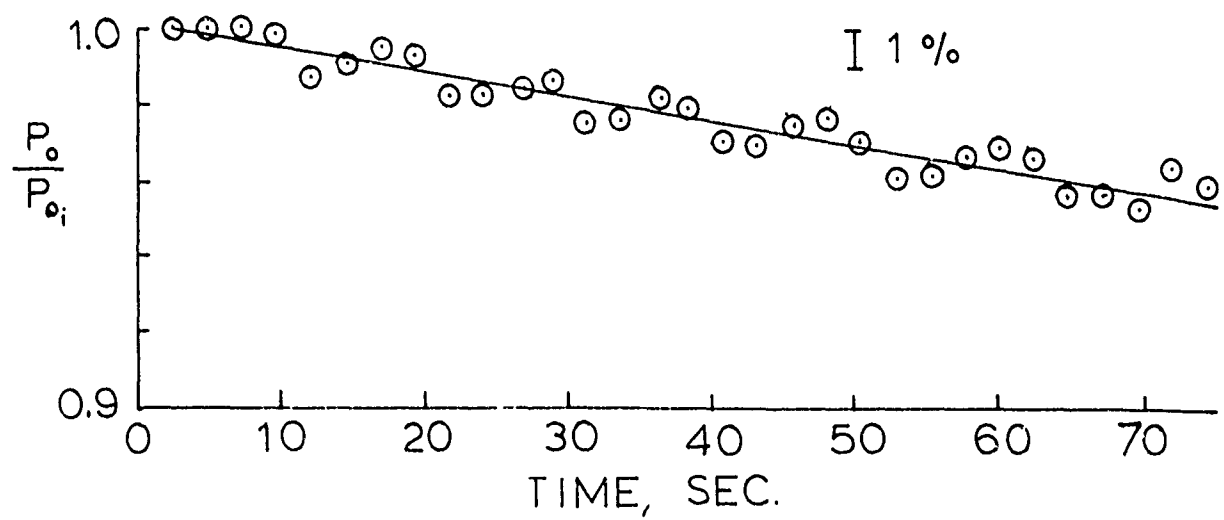


FIGURE 16. VARIATION IN STAGNATION PRESSURE AT TEST SECTION INLET.

period control-value hunting, of approximately 10 seconds duration, is also evident in these results. However, a short period deviation from a linear decay is always less than one percent. In order to minimize the errors due to stagnation pressure variations all other pressures are normalized by stagnation pressures measured periodically during the test. Each pressure is measured within less than one second of the time that its normalizing stagnation pressure is measured. This is an important advantage of the programmed data retrieval system. Consequently, errors due to stagnation pressure variations are believed to be less than one percent (i.e., the maximum deviation from a smooth decay curve).

#### Diffuser Performance

Pressure distributions along the shock diffuser for four nozzle inlet stagnation pressures are represented in Figure 17 where the local surface pressure,  $P$ , is normalized by the upstream stagnation pressure,  $P_0$ . For stagnation pressures in excess of 3730 mmHg the shock train begins at more than 30 base diameters downstream of the base plane. The shock pressure rise starts abruptly, as for fully developed pipe flow,<sup>(23)</sup> and has no effect on the pressures near the base. With the pressure reduced to 3080 mmHg the shock train starts ahead of the base plane, near the nozzle exit. The minimum stagnation pressure with shock deceleration in the diffuser as computed using one-dimensional flow analyses, neglecting surface friction but including base drag, is 3180 mmHg. This is in good agreement with the experimental result. It is of particular interest that the shock train is apparently completed in less than 10 diffuser diameters even though the core of the diffuser flow contains the base wake. This is slightly less (approximately 20 percent) than that reported in Reference 23 on the basis

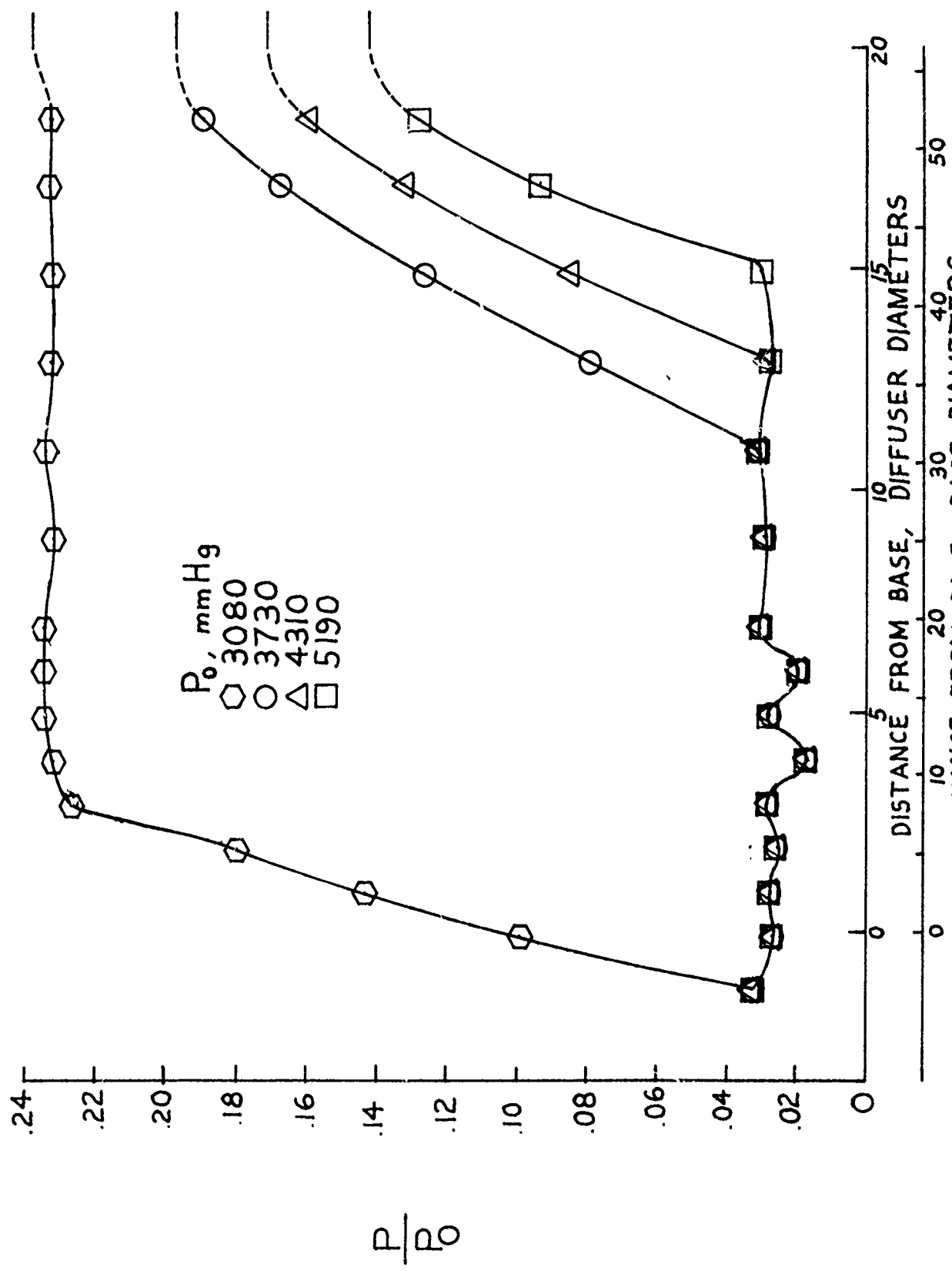


FIGURE 17. DIFFUSER PRESSURE DISTRIBUTIONS

of experiments with a smaller scale, developed pipe flow.

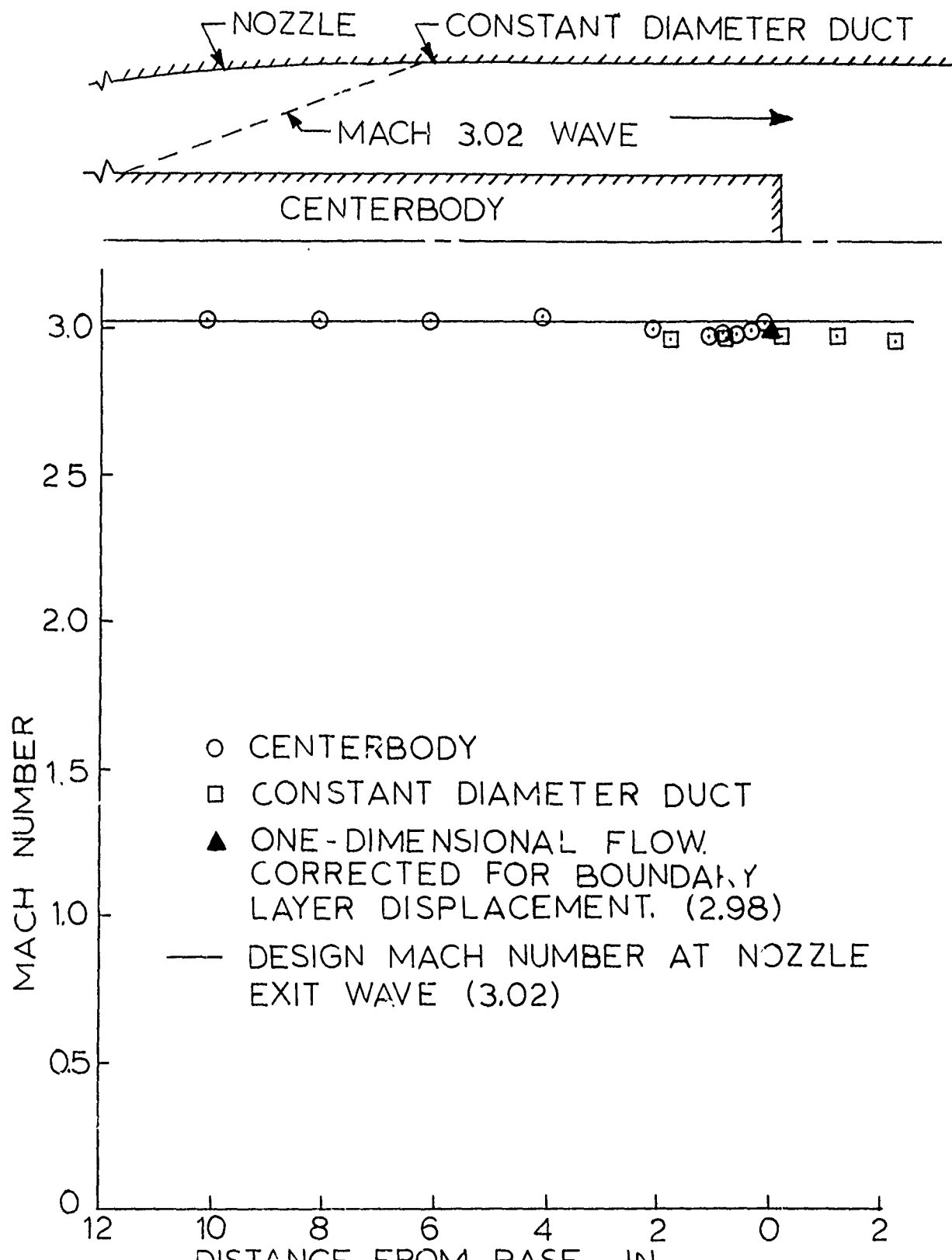
The pressure variations slightly downstream of the base plane are due to the base expansion and wake recompression waves. The proof that these pressure variations do not affect the near wake will be presented in the next chapter.

#### Test Section Flow

Axial distributions of Mach-numbers along the centerbody from near the nozzle exit to the base plane and along the outer, constant-diameter duct from two inches upstream to two inches downstream of the base plane are shown in Figure 18. The Mach number on the centerbody near the nozzle exit is reasonably close to the design value of 3.02. The Mach number decreases slightly toward the base plane due to the boundary layer growth. Near the base plane the Mach numbers both the outer ducting and the centerbody are in good agreement with the value of 2.98 computed assuming one-dimensional flow with the flow area corrected for the theoretical values of the boundary-layer displacement thickness. There is also evidence of a slight Mach number increase on the centerbody immediately upstream of the base, due to the expansion at the base shoulder.

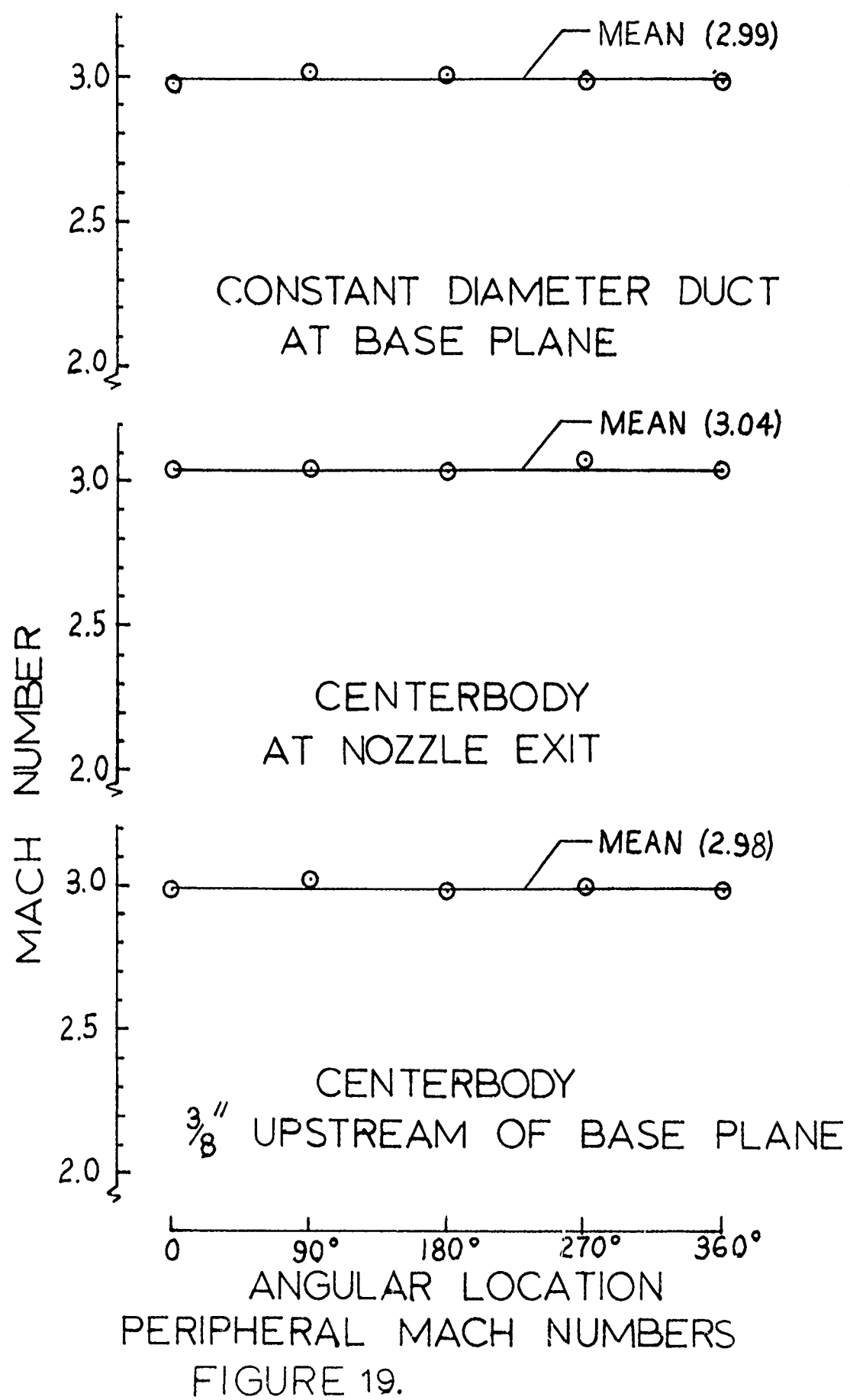
The reference Mach number,  $M_1$ , on the cylindrical centerbody upstream of the base plane will be taken to be 2.98, corresponding to the one-dimensional flow value, for all subsequent data reduction analyses.

Peripheral distributions of Mach numbers on the centerbody and outer ducting are illustrated in Figure 19. The data points are from one typical run. Each of the mean lines, however, are based on the results of six runs conducted on three days. The maximum deviation of any data point from the mean line is only one percent. Furthermore, the mean value of the Mach



AXIAL MACH NUMBER DISTRIBUTIONS

FIGURE 18.



number on the centerbody near the nozzle exit is only 0.5 percent higher than the design value. In addition, the mean values of the Mach number on the centerbody and the outer ducting near the nozzle exit plane are in good agreement with the theoretical, one-dimensional flow value of 2.98.

Ratios of the centerbody surface temperature near the base plane to the freestream stagnation temperature,  $T_{o_1}$ , are presented in Figure 20 for two typical runs. For both of these runs, the test period, during which the temperatures were sampled many times, was approximately 100 seconds. For Run 1, the test period started immediately after the upstream flow was stabilized. Consequently, the surface temperature is initially slightly higher than the stagnation temperature. For Run 2, the test period started about 50 seconds after the upstream flow was stabilized. Other data were acquired during this initial 50 seconds. For comparison, the corresponding temperature ratio for an adiabatic wall with a typical flat-plate recovery factor of 0.9 is included on Figure 20. A comparison of this adiabatic wall temperature ratio with the data shows that adiabatic flow is essentially obtained at the end of these two runs. Throughout the entire test periods the ratio of the actual wall temperature to the adiabatic wall temperature is only slightly greater than one. Correspondingly, the effects of heat transfer to the centerbody on the base flow are expected to be small.

#### Data Accuracy and Repeatability

The pressure transducers are periodically calibrated against accurate dead-weight testers and calibration curves are used in all data retrieval programs. Typical calibration results for the strain-gage transducer and one variable-capacitance Barocel transducer are presented in Figure 21. These results are included to emphasize the quality of the calibration curves

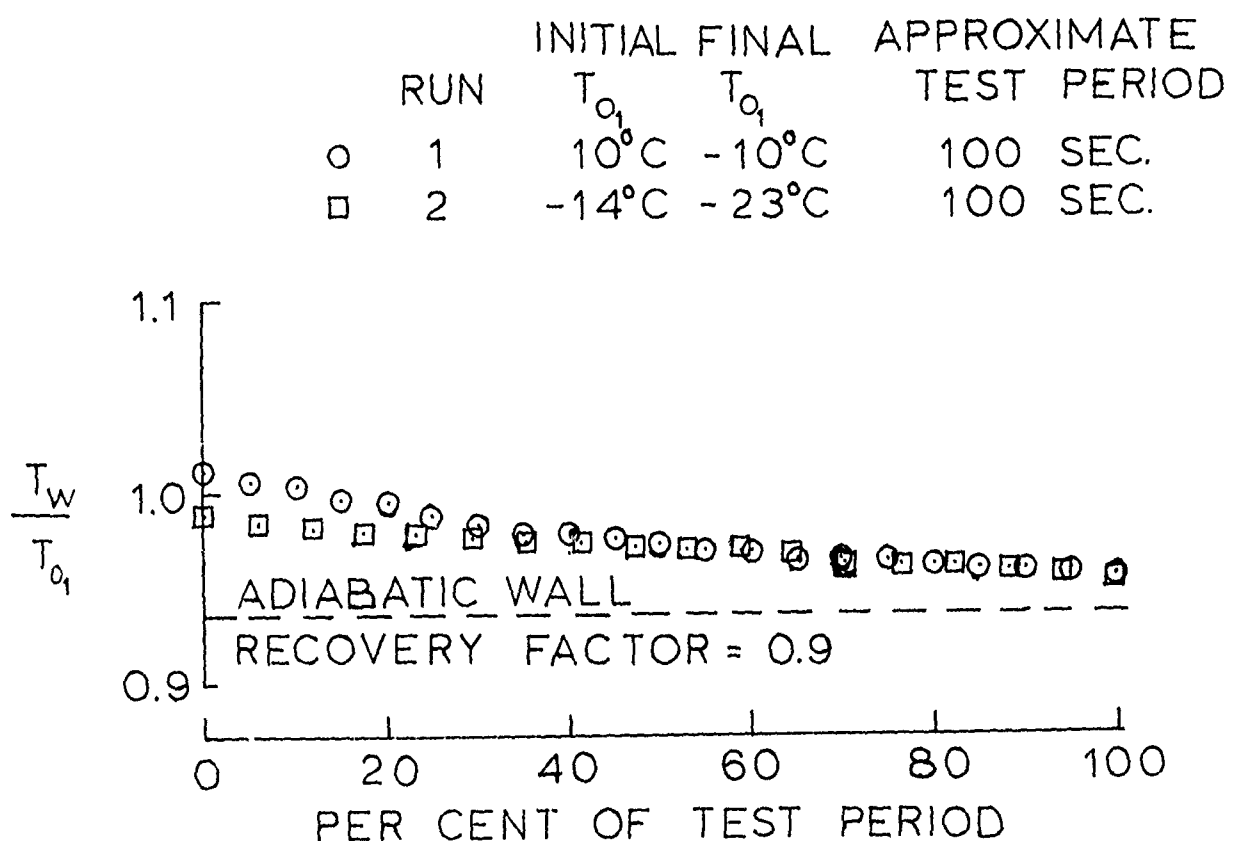


FIGURE 20. TYPICAL VARIATIONS IN THE RATIOS OF CENTERBODY SURFACE TO FREESTREAM STAGNATION TEMPERATURES.

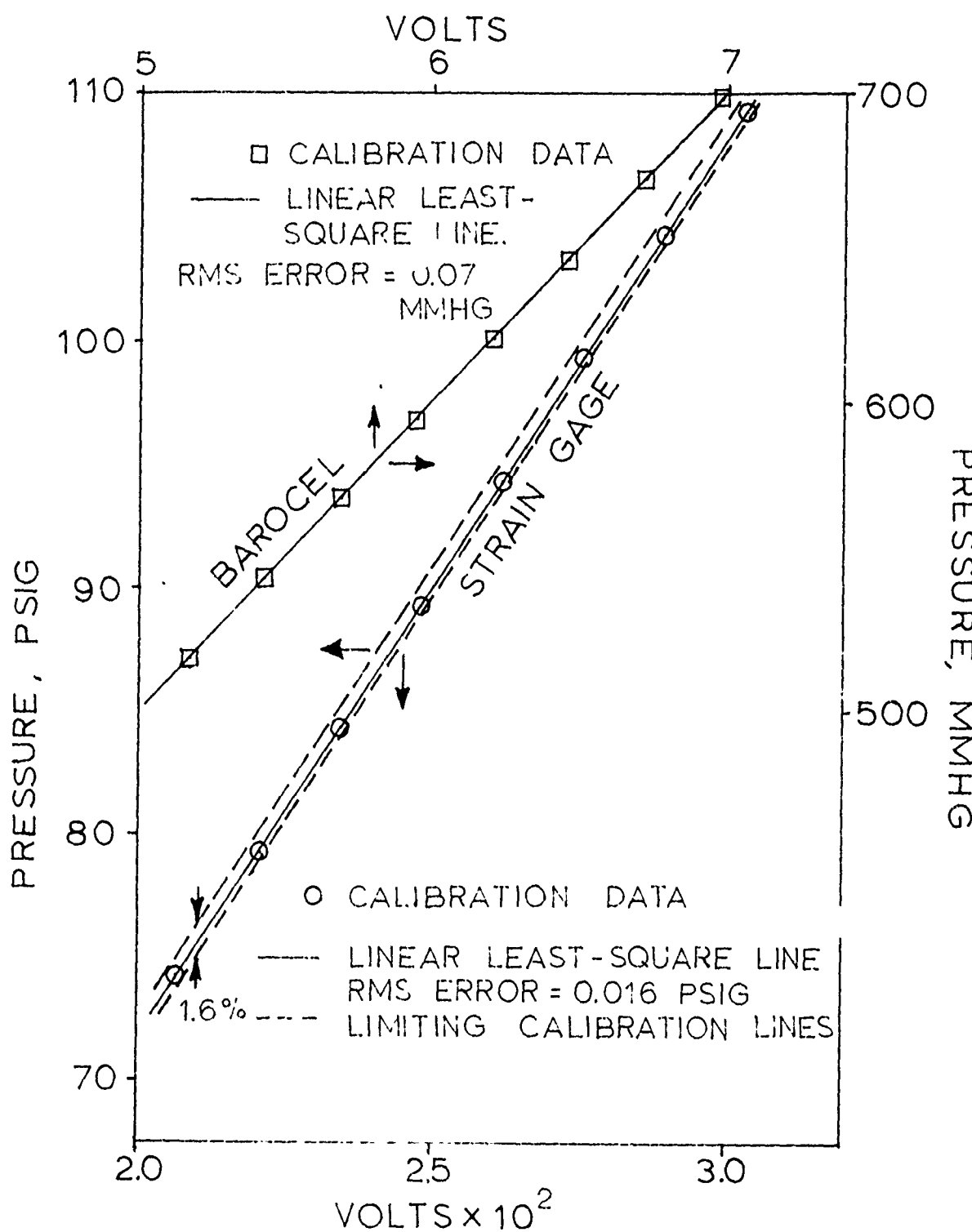


FIGURE 21. CALIBRATION RESULTS FOR PRESSURE TRANSDUCERS

and the expected accuracies of the data. The root-mean-square error of the data deviations from a linear least-square line is negligible in both cases. The only significant source of error is a shift in calibrations with both time and cycling of the pressure loads on the transducers. Calibrating for the cycling effects is impossible for tests of different durations and pressure sampling demands. The dashed lines on Figure 21 show the upper and lower limits of the calibration lines which have been obtained for the strain-gage transducer over a period of four months and with different transducer loading schedules. The total change is only 1.6 percent at the lower pressures. The maximum change for the two Barocel transducers over the same period of time has been only 0.4 percent in the pressure range of interest. Since the Barocel transducers measure the low test-section pressures using an atmospheric reference, this change is amplified to a maximum of no more than three percent of the absolute pressure. However, because calibration curves are periodically obtained for subsequent use in the data retrieval programs, it is believed that all absolute pressures are at least obtained within an accuracy of  $\pm 1$  percent, the major source of error being the changes with cycling, which varies from tests to tests.

As previously discussed, variations in the nozzle inlet stagnation pressure also introduce slight errors which are believed to be less than  $\pm 1$  percent. The coupling of this error with that of the transducers yields a maximum pressure error of  $\pm 2$  percent. This is considered to be a conservative estimate. The effects of pressure lag due to the transducer and line volumes are negligible since minimum pressure scanning rates are established from lag tests of the complete pressure measuring systems.

Figure 22 presents Mach number distributions along the centerbody upstream of the base as obtained in four runs on three days. These typical results are included to illustrate the repeatability of the test data and to support the conclusions concerning the data accuracies. The Mach number variations are a maximum of  $\pm 0.4$  percent from the mean. The corresponding pressure variations are  $\pm 1.6$  percent. These largest variations occur near the base plane where other measurements have shown that the flow conditions are most sensitive to small changes. Upstream of this region these and other measurements indicate a maximum pressure variation of about  $\pm 1$  percent. It is also important to note that variations shown on Figure 22 are apparently random.

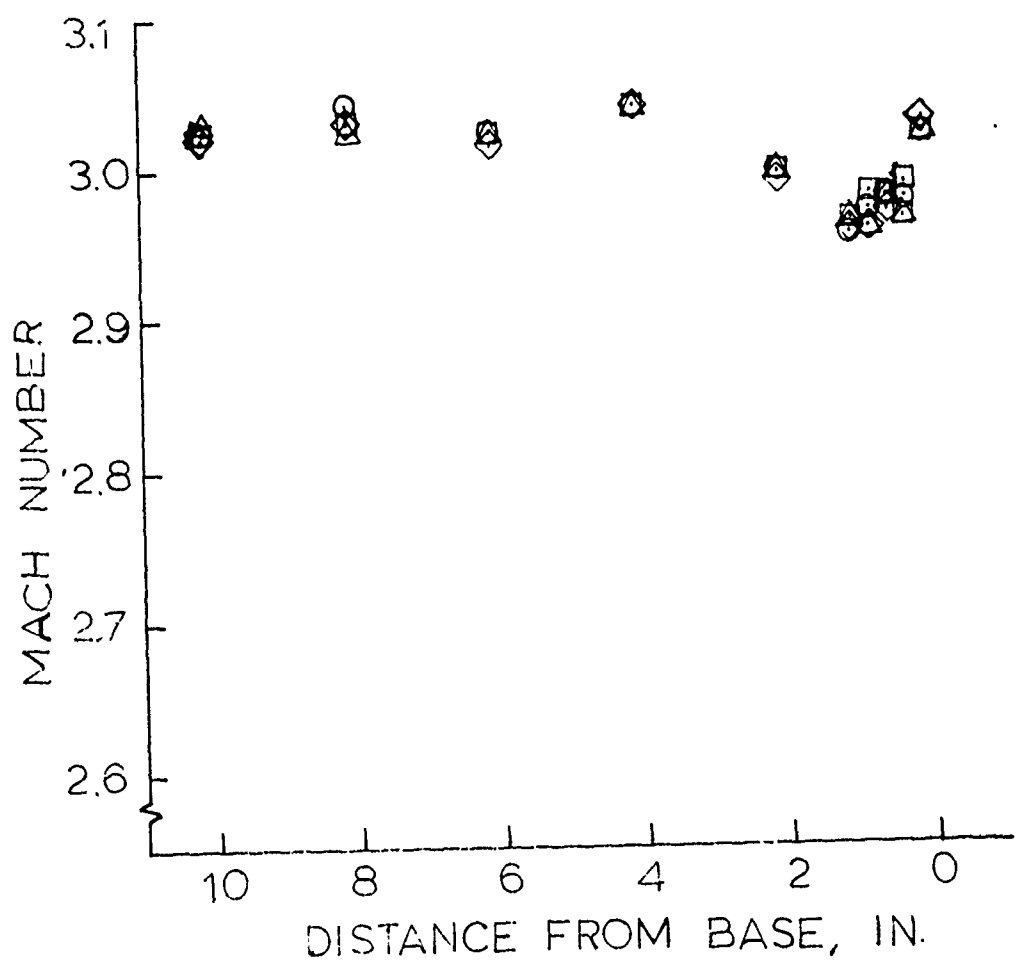


FIGURE 22. COMPARISONS OF RESULTS OF REPEAT TESTS

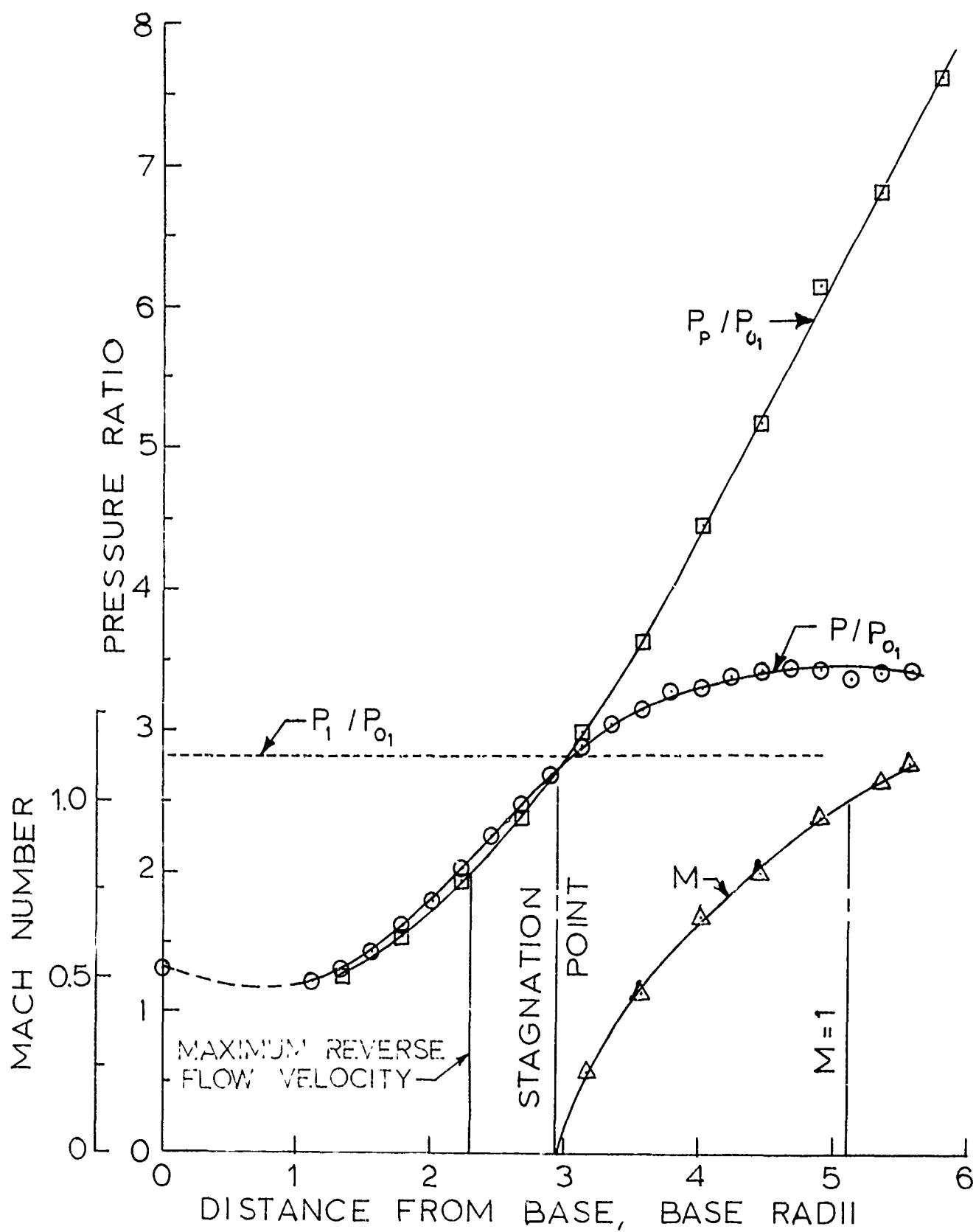
## CHAPTER IV

## BASE FLOW RESULTS

To date, all base flow data have been obtained using constant-diameter ducting downstream of the nozzle. Thus, no external disturbances, other than those due to the boundary layer on the centerbody, have been impressed on the near wake. For the tests, the ratio of the boundary layer momentum thickness on the centerbody at the base shoulder, as computed using the theory of Reference 22, to the base radius is 0.0135 for a flow Reynolds number based on the centerbody diameter of  $3.8 \times 10^6$ . The base flow results which have been obtained to date are presented in this Chapter. These results provide the basis for comparisons with existing results as well as with later test results with base flow disturbances.

Distributions of the static and pitot probe pressures along the wake centerline downstream of the base are presented in Figure 23.  $P_1$  and  $P_{01}$  are the static and stagnation pressure in the free-stream flow immediately ahead of the base plane,  $P$  and  $M$  are the static pressure and Mach number along the wake centerline, and  $P_p$  is the measured pitot probe pressure. All the pressures have been normalized by the stagnation pressure measured during the tests in order to minimize the effects of stagnation pressure drifts.

The rear stagnation point, as determined by the intersection of the pitot and static probe pressures, is located approximately 3 base radii downstream of the base plane. In the reverse flow region nearer the base, the pitot probe measures a probe base pressure which is lower than the local static pressure. The maximum difference between these two pressures



PRESSURE AND MACH NUMBER DISTRIBUTION  
ALONG WAKE CENTERLINE  
FIGURE 23.

occurs at the point where the reverse flow velocity is a maximum. This occurs at approximately 2.3 base radii from the base plane.

The centerline Mach number distribution downstream of the rear stagnation point, as computed from the ratios of the pitot and static probe pressures, is also plotted in Figure 23. The centerline Mach number increases smoothly and becomes sonic at about 5 base radii downstream of the base plane. The wake choking or critical point lies ahead of this sonic condition. Disturbances downstream of this sonic point cannot propagate upstream into the near wake.

The static to stagnation pressure ratio upstream of the base expansion has also been included on Figure 23 for comparison with the centerline static pressure distribution in order to illustrate the overcompression that occurs near the wake neck for axisymmetric base flow. This overcompression is primarily responsible for the base pressures being higher with axisymmetric bodies than with two-dimensional bodies. For the present case, the peak pressure along the wake centerline is 23 percent higher than the upstream pressure.

Figure 24 is included to emphasize that the base pressure is independent of the probe position.  $P_b$  is the base static pressure (in this case,  $P_b$  is measured at the center of the base) and  $\bar{P}_b$  is the numerical average of  $P_b$  for all measurements in which the probe was located in the subsonic near wake. The percent variation in the base pressure from the mean base pressure is plotted for each pitot probe location for which the probe is in the subsonic near wake. For the two points with the probe tip nearest the base the 0.125 inch probe shank also projects into the subsonic flow region. However, even the diameter of this shank is less than six percent of the base diameter. The small differences shown on Figure 24 are within the expected data accuracy as previously discussed.

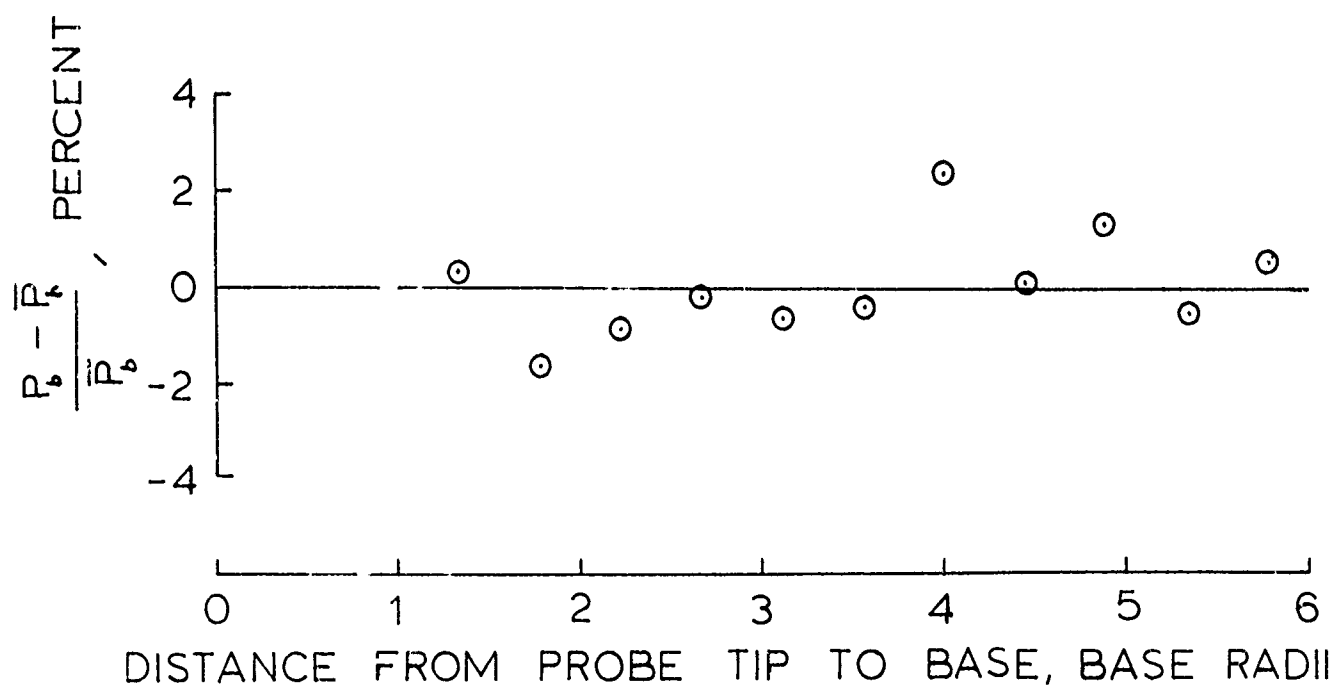
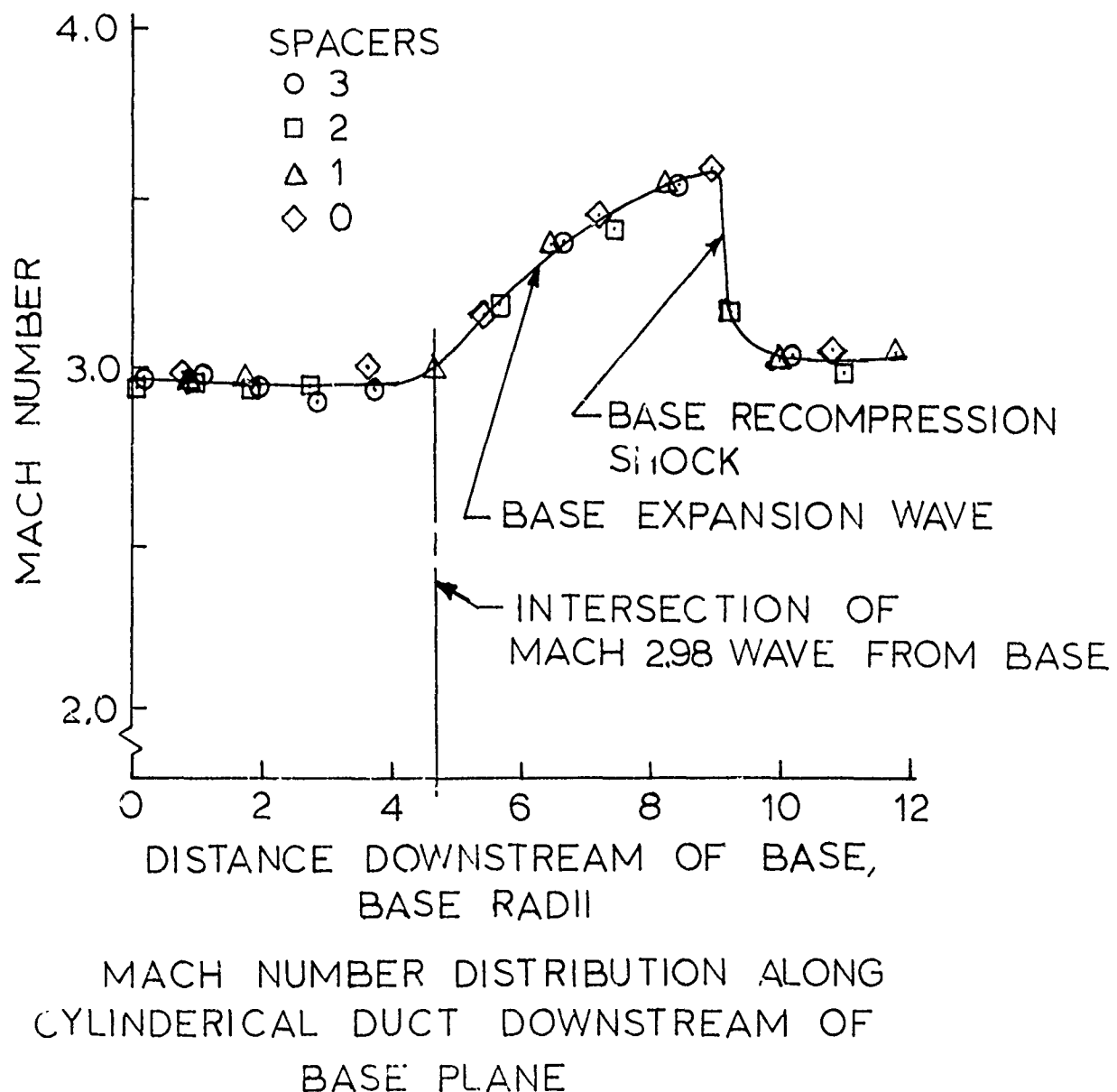


FIGURE 24. VARIATION IN BASE PRESSURE  
WITH PITOT PROBE POSITION

The Mach number distribution on the outer cylindrical ducting downstream of the base plane is shown in Figure 25. These Mach numbers were computed from the ratios of the surface static pressure and the upstream stagnation pressure. All three spaces (between the nozzle and constant diameter duct) were used for these tests in order to displace the static pressure taps. The Mach number remains constant until the expansion wave from the base shoulder intersects the ducting. This expansion starts at about five base radii downstream of the base plane. At approximately nine base radii downstream, the Mach number decreases sharply as a result of the wake recompression waves which have apparently coalesced into a shock wave. As shown in Figure 23, this recompression, which propagates from the wake boundary, starts at about one base radius downstream of the base. Subsequent reflections of these expansion and compression waves account for the pressure variations farther downstream in the diffuser as shown in Figure 17. However, reflections from the outer cylinder cannot intersect the wake upstream of the sonic point on the wake centerline.

Radial and peripheral base pressure distributions are presented in Figure 26. Again the pressures are normalized by the upstream stagnation pressure. Each data point on Figure 25 represents the mean value for five tests. The five pressures for each point are all within  $\pm 1.5$  percent of the mean value, and thus, within the expected limits of accuracy. As shown in the upper part of the figure, the base pressure increases with the radius. From the center to 0.67 base radii the pressure increases by 9 percent. Reid and Hastings<sup>(4)</sup> reported similar trends for axisymmetric bodies with cylindrical, conical, and parabolic afterbodies at Mach 2.0. However, their radial pressure gradients, which averaged out the peripheral asymmetries by using four radial surveys at  $90^\circ$  intervals, were somewhat



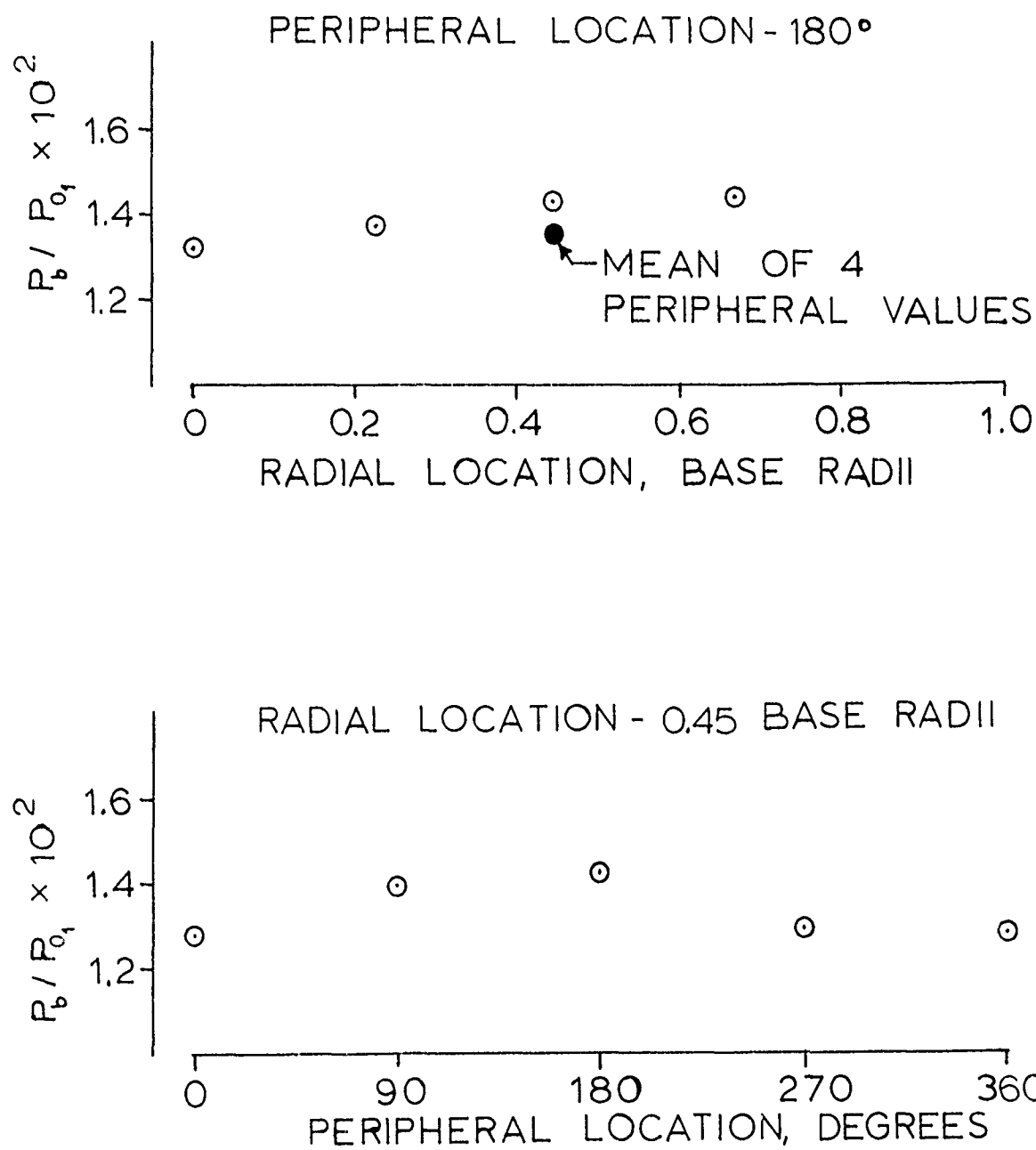


FIGURE 26. BASE PRESSURE DISTRIBUTIONS

smaller than those of Figure 26. Apparently a major portion of the radial pressure increase with the present tests may be attributed to a slight flow asymmetry as shown in the lower part of Figure 26. This figure shows the peripheral variation in the base pressures at 0.45 base radii from the center. To illustrate the effect of the peripheral variations, the mean value of these four peripheral pressures is included as the solid point on the upper figure. Apparently, the average radial pressure gradient is reduced by the peripheral variations.

The numerical average of the base pressure ratios on Figure 26 is  $\bar{P}_b/P_{o_1} = 1.357 \times 10^{-2}$ . This corresponds to a mean base pressure coefficient of  $\bar{C}_{p_b} = -0.083$ , based on the average Mach number upstream of the base expansion of  $M_1 = 2.98$ . This is in good agreement with the results of free-flight and wind-tunnel tests for axisymmetric projectiles of high ineness ratio as summarized by Love<sup>(25)</sup> and Murthy and Osborn<sup>(26)</sup>.

The Reynolds number was varied over a small range in one test series by varying the upstream stagnation pressure over the range of about 70 to 150 psia. The base pressure results are summarized in the following table. The mean values of the base pressure and pressure coefficient for each test run are based on the numerical average of the seven base pressure measurements. The Reynolds number is based on the diameter of the base. The differences for this small Reynolds number range are within the accuracy of the data.

Run	$Re \times 10^{-6}$	$\bar{P}_b/P_o \times 10^2$	$\bar{C}_{p_b}$
1	2.48	1.368	-0.0824
2	2.70	1.352	-0.0833
3	3.26	1.366	-0.0825
4	4.74	1.366	-0.0825
5	5.19	1.338	-0.0841

## REFERENCES

1. Baker, W. T., Davis, T., and Matthews, S., 1951, The John Hopkins' University, Applied Physics Laboratory CM-673.
2. Scanland, T. S., and Hebrank, W. H., 1952, Ballistic Research Laboratories, Memorandum Report No. 596.
3. Townsend, L. H. and Reid, J., 1964, Supersonic Flow, Chemical Processes and Radiative Transfer, p. 135, Macmillan.
4. Davis, L. R., 1968, AIAA, J., 6, 843.
5. Fox, H., Zakkay, V., and Sinha, R., 1966, New York University, NYU-11-66-63.
6. Reeves, B. L. and Lees, L., 1965, AIAA J., 3, 2061.
7. Scott, C. J. and Eckert, E. R. G., 1966, AGARD Conference on Separated Flows, Pt. I, p. 429.
8. Gazley, C. G., Jr., 1956, The RAND Corporation, RM-1892.
9. Wilmarth, W. W., 1957, The RAND Corporation, RM 2078
10. Chu, B. T., 1955, NACA TN 3411.
11. Billig, F. S., 1967, The John Hopkins University, Applied Physics Laboratory, TG912.
12. Strahle, W. C., 1969, Twelfth Symposium (International) on Combustion, p. 1163, The Combustion Institute.
13. Serafini, J. S., Dorsch, R. G., and Fletcher, E. A., 1957, NACA RME 57E15.
14. Crocco, L. and Lees, L., 1952, J. Aerospace Sci, 19, 649.
15. Alber, S. E., 1967, Ph.D. Dissertation, California Institute of Technology.
16. Korst, H. H., Page, R. H., and Childs, M. E., 1955, University of Illinois, ME Technical Note 392-2.

17. Smithy, W. J. H., 1974, Ph.D. Dissertation, Naval Postgraduate School.
18. Horn, N. P., 1974, M.S. Thesis, Naval Postgraduate School.
19. Smithy, W. J. H. and Fuhs, A. E., 1974, Workshop on Aerodynamics of Base Combustion, Perdue University.
20. Bradshaw, P., 1965, J. Fluid Mech., 22, part 4, 679.
21. Hall, I. M., 1962, Quart. Journ. Mech. and Applied Math., XV, Part 4, 487.
22. Cebeci, T., Smith, A. M. O., and Wang, L. C., 1969, McDonnel Douglas Report No. DAC-67131.
23. Neumann, E. P. and Lustwerk, F., 1949, J. Fluid Mech., 195.
24. Reid, J. and Hastings, R. C., 1959, A. R. C. 21, 707.
25. Love, Eugene S., 1957, NACA TN 3819, (1957).
26. Murthy, S. N. B. and Osborn, J. R., 1973, BRL, C. R. 113.

UNCLASSIFIED

SECURITY CLASSIFICATION OF THIS PAGE (If Different From Above) \_\_\_\_\_ Date Entered \_\_\_\_\_

(19) REPORT DOCUMENTATION PAGE		READ INSTRUCTIONS BEFORE COMPLETING FORM	
1. REPORT NUMBER AFOSR - TR - 76 - 0563	2. GOVT ACCESSION NO.	3. RECIPIENT'S CATALOG NUMBER	
4. TITLE (and Subtitle) EXPERIMENTS AND ANALYSIS RELATED TO EXTERNAL BURNING FOR PROPULSION,		5. TYPE OF REPORT & PERIOD COVERED INTERIM <i>rept.</i> FEB 75 - JAN 76	
7. AUT. ORG. E. JUBBARTT G. STRAHLE H. NEALE		8. CONTRACT OR GRANT NUMBER(s) AF- AFOSR 2794-75	
9. PERFORMING ORGANIZATION NAME AND ADDRESS GEORGIA INSTITUTE OF TECHNOLOGY SCHOOL OF AEROSPACE ENGINEERING ATLANTA, GEORGIA 30332		10. PROGRAM ELEMENT, PROJECT, TASK AREA & WORK UNIT NUMBERS 681308 9711-02 61102F	
11. CONTROLLING OFFICE NAME AND ADDRESS AIR FORCE OFFICE OF SCIENTIFIC RESEARCH/NA BUILDING 410 BOLLING AIR FORCE BASE, D C 20332		12. REPORT DATE Mar 1976	12. NUMBER OF PAGES 60
14. MONITORING AGENCY NAME & ADDRESS (if different from Controlling Office) AF-9411 17 941102		15. SECURITY CLASS. (of this report) UNCLASSIFIED	
16. DISTRIBUTION STATEMENT (of this Report) Approved for public release; distribution unlimited.		15a. DECLASSIFICATION DOWNGRADING SCHEDULE	
17. DISTRIBUTION STATEMENT (of the abstract entered in Block 20, if different from Report)			
18. SUPPLEMENTARY NOTES			
19. KEY WORDS (Continue on reverse side if necessary and identify by block number) EXTERNAL BURNING PROPULSION BASE FLOW SUPERSONIC FLOW WIND TUNNEL			
20. ABSTRACT (Continue on reverse side if necessary and identify by block number) The results of first year's efforts on an experimental base flow program are reported. The design and checkout for a Mach 3.0 axisymmetric wind tunnel with a model base diameter of 2.25 inches is described, as well as the automated data acquisition system. Experiments are reported on detailed static pressures for the diffuser wall, model wall and base and near wake. Temperature measurements are presented to establish a near adiabatic wall condition. The relationship between the experimental program and propulsive external burning is discussed.			